

# Quaternary surface ruptures of the inherited mature Yangsan Fault: implications for intraplate earthquakes in Southeastern Korea

Sangmin Ha<sup>1,2</sup>, Hee-Cheol Kang<sup>1,3</sup>, Seongjun Lee<sup>1,4</sup>, Yeong Bae Seong<sup>2</sup>, Jeong-Heon Choi<sup>5</sup>, Seok-Jin Kim<sup>5,6</sup>, Moon Son<sup>1</sup>

5 <sup>1</sup>Department of Geological Sciences, Pusan National University, Busan 46241, South Korea

<sup>2</sup>Department of Geography Education, Korea University, Seoul 02841, South Korea

<sup>3</sup>Institute of Geohazard Research, Pusan National University, Busan 46241, South Korea

<sup>4</sup>Department of Geotechnology & Infrastructure, Byucksan Engineering, Seoul 08380, South Korea

<sup>5</sup>Research Center of Earth and Environmental Sciences, Korea Basic Science Institute, Chungbuk 28119, South Korea

10 <sup>6</sup>Conservation Science Division, National Research Institute of Cultural Heritage, Daejeon, 34122, South Korea

*Correspondence to:* Moon Son (moonson@pusan.ac.kr)

**Abstract.** Earthquake prediction in intraplate regions, such as the Korean Peninsula, is challenging due to the complexity of fault distributions. This study employed diverse methods and data sources to investigate Quaternary surface rupturing along the Yangsan Fault, aiming to understand its long-term earthquake behavior. Paleoseismic data of the Byeogye section (7.6  
15 km) of the Yangsan Fault are analyzed to provide insights into earthquake parameters (i.e., timing, displacement, and recurrence intervals) as well as structural patterns. Observations from five trench sites indicate at least six faulting events during the Quaternary, with the most recent surface rupturing occurring approximately 3,000 years ago. These events resulted in a cumulative horizontal displacement of 76 m and a maximum estimated magnitude of  $M_w$  6.7–7.1. The average slip rate of  $0.13 \pm 0.1$  mm/yr suggests a quasi-periodic model with possible recurrence intervals exceeding 13,000 years.  
20 Structural patterns indicate the reactivation of a pre-existing fault core with top-to-the-west geometry, causing a dextral-slip with a minor reverse component. This study underscores the several surface ruptures with large earthquakes along the inherited mature Yangsan Fault, since at least the Early Pleistocene, offering critical insights for seismic hazard and a broader understanding of intraplate earthquake dynamics, enhancing earthquake prediction effort.

25 **Short summary.** Unlike episodic plate boundary earthquakes, their randomness makes predicting intraplate earthquakes challenging. This study aids in understanding intraplate earthquake behavior by analyzing paleoearthquake records of the Yangsan Fault in Korea. Five trench sites revealed six Quaternary earthquakes, the latest 3,000 years ago, with  $M_w$  6.7–7.1. The right lateral fault has a 0.13 mm/yr slip rate, and a recurrence interval over 13,000 years, continuously active since the Quaternary.

30

## 1 Introduction

Earthquake prediction is challenging, and large earthquakes with surface ruptures significantly damage infrastructure (Geller et al., 1997; Wyss, 1997; Crampin and Gao, 2010; Woith et al., 2018). To predict large earthquakes, it is necessary to identify the pattern of earthquake occurrences, which can be periodic, quasi-periodic, and random (Shimazaki and Nakata, 1980; 35 McCalpin, 2009). Earthquakes can be categorized as interplate (plate boundary) or intraplate (mid-continental) based on their tectonic location (England and Jackson, 2011; Liu and Stein, 2016). Numerous studies have identified relatively "predictable" cycles, patterns, causes, magnitudes, and epicentres in the interplate, where earthquakes are more frequent, leading to improved earthquake preparedness (e.g., San Andreas Fault, Nankai trough; Powell and Weldon II, 1992; Murray and Langbein, 2006; Smith and Sandwell, 2006; Uchida and Burgmann, 2019; Obara and Kato, 2024).

40 Large earthquakes in the intraplate occur less frequently than in the interplate but can have devastating impacts (e.g., 1556 Huaxian earthquake-M 8.0, 1976 Tangshan earthquake-M<sub>w</sub> 7.8, 1811-1812 New Madrid earthquake, 2001 Gujarat earthquake-M<sub>w</sub> 7.6, 2011 Virginia earthquake-M 5.8; Min et al., 1995; Johnston and Schweig, 1996; Hough et al., 2000; Hough and Page, 2011; Wolin et al., 2012). Large intraplate earthquakes have recently received considerable attention and researchers are attempting to understand them based on insights obtained from interplate earthquakes (England and Jackson, 2011; Liu and 45 Stein, 2016; Talwani, 2017). However, intraplate earthquakes exhibit complex spatiotemporal patterns that do not follow general interplate earthquake pattern models (Liu and Stein, 2016; Talwani, 2017). This can partly be explained by the poor catalogue due to their slow slip rates (<1 mm/year) and long recurrence intervals (>1,000 yr). The faults in the intraplate region have a complex distribution rather than those in the interplate region and tend to be selectively reactivated in response to far-field stress (Liu and Stein, 2016; Talwani, 2017).

50 To understand the unpredictable patterns of intraplate earthquakes, it is necessary not only to collect robust paleoseismic data but also to find connections between paleoseismic data and structural features such as the relationship between geometry and the in-situ stress regime, fault kinematics controlled by pre-existing structure. Korea, located on the intraplate, has experienced very few damaging earthquakes since instrumented seismic monitoring began. However, medium-sized earthquakes have caused damage ~~to people~~ near the epicentres and raised earthquake awareness (e.g., the 2016 Gyeongju earthquake; the 2017 55 Pohang earthquake; Kim et al., 2018; Woo et al., 2019). Despite calls for realistic earthquake preparedness, seismic research in South Korea remains at an early stage compared to neighbouring countries on plate boundaries, such as Japan and Taiwan. Basic seismic hazard assessment requires the acquisition of robust paleoseismic data (Reiter, 1990; Gurpinar, 2005; McCalpin, 2009). The reduction of paleoseismic uncertainty necessitates an expanded dataset, which in turn demands a significant volume of data. Various methods can be employed to efficiently detect Quaternary faults and obtain robust paleoseismic parameters.

60 Although this need has been recognized, until recently, paleoseismology studies in Korea have mostly been based on a single trench except ~~recent~~ a few recent studies (e.g., Kim et al., 2023). Earthquakes in South Korea appear to follow the quasiperiodic behavior of intraplate earthquakes (Kim and Lee, 2023). To unravel this quasiperiodic pattern of an intraplate fault, it is necessary to collect paleoseismic data from multiple faults with Quaternary surface rupturing to complete the puzzle. The

65 Yangsan Fault is one of the vital intraplate faults in Korea that could solve this puzzle, with recent reports of Quaternary surface rupture (e.g., Kim et al., 2023), but many unknowns remain. In this study, we try to provide clues to the pattern of earthquake behavior of the Yangsan Fault.

70 This study ~~seeksought~~ to trace the distribution of the Quaternary surface rupturing during the Holocene and obtain fundamental paleoseismic data on the Yangsan Fault. To achieve this, we ~~applied~~ multiple methods to identify traces of Quaternary surface ruptures with higher accuracy and interpret a highly robust paleoseismic synthesis from the extensive data collected (e.g., five  
75 trenches and about ~30 numerical ages). We ~~focused~~ on the Byeokgye section (Kim et al., 2022) in the southern part of the northern Yangsan Fault, a major tectonic line in southeastern Korea, to create a geological map and select trench sites through fieldwork. This study aims to reveal 1) robust paleoseismic data, filling gaps in prior surface rupture documentation, 2) Quaternary reactivation features of intraplate mature fault zones, and 3) the spatiotemporal surface rupturing pattern of the Yangsan Fault. The results of this study can be used as essential inputs for seismic hazard assessment and to understand the Quaternary rupturing patterns of the Yangsan Fault.

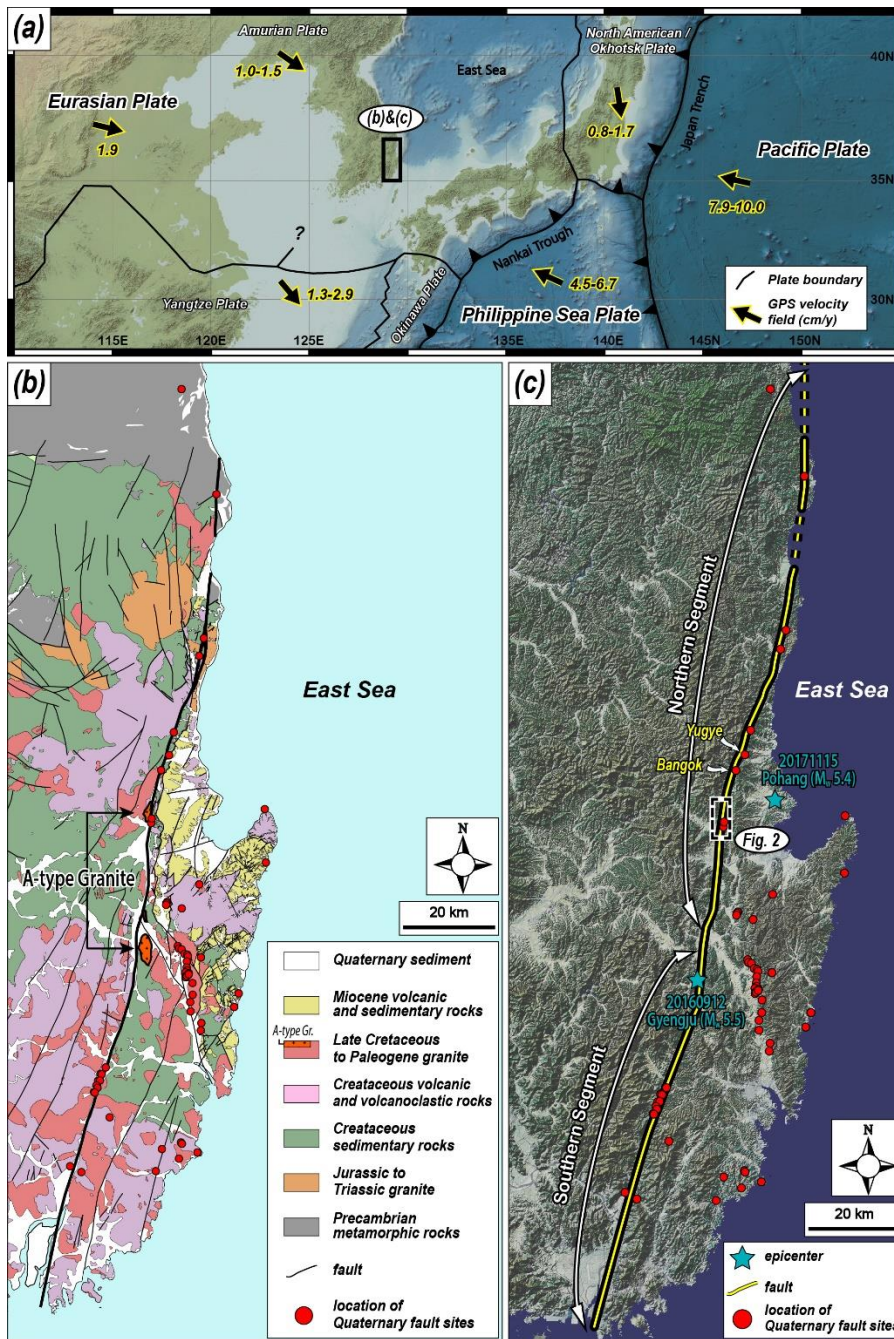


Figure 1: Regional study area maps. (a) Tectonic map of East Asia showing plate boundaries and their velocities (modified from DeMets et al., 1990, 1994; Seno et al., 1993, 1996; Heki et al., 1999; Bird, 2003; O’Nelli et al., 2005; Schellart & Rawlinson, 2010; M.-C. Kim et al., 2016). The black arrow indicates the moving direction of each plate. (b) Regional geological map of SE Korea (modified from Chang et al., 1990; Kim et al., 1998; Hwang et al., 2007a, 2007b; Son et al., 2015; Song, 2015; Kang et al., 2018). The thick black line indicates the Yangsan Fault, and the 21 km dextral offset of the Yangsan Fault is interpreted by the distribution of a-type granite. (c) Topographic satellite image map of SE Korea and recent epicentres. The Yangsan Fault is divided into two segments (modified from Kim et al., 2022; 2023b) and the study area is located in the southern part of the northern segment.

## 2 Tectonic and geological setting

### 85 2.1 Regional seismotectonic setting of Korea

The Korean Peninsula is located ~~at on the Amurian Plate, which was once thought to be part of~~ the eastern margin of the Eurasian Plate (Fig. 1a; e.g., Bird, 2003; Calais et al., 2006; Argus et al., 2010; Ashurkov et al., 2011). The relative frequency of earthquakes in Korea is low compared with other ~~regioncountries~~ on nearby plate boundaries, such as Japan, China, Taiwan, and the Philippines (KMA, 2022). While paleoseismology, archaeoseismology, and historical seismicity studies indicate that

90 large ( $M \geq 7$ ) earthquakes occurred in the past, medium-sized ( $M \geq 5$ ) instrumental earthquakes have been occasionally observed since the onset of seismic instrument measurements (Lee, 1998; Lee and Yang, 2006; Han et al., 2016; Kim et al., 2016; 2018; 2020b). Currently, the Korean Peninsula is under a maximum horizontal stress of the E-W to ENE-WSW direction, which is the result of the combined effects of the subduction of the Pacific and Philippine Sea Plates and eastward-propagating far-field stress from India-Eurasia collision (Park et al., 2006; Kim et al., 2016; Kuwahara et al., 2021). GNSS studies show that the

95 Korean Peninsula has a velocity field of about 3 cm/yr ~~towardins~~ the WNW direction (Ansari and Bae, 2020; Sohn et al., 2021; Kim and Bae, 2023). Recent short-term (2 year) GNSS studies on the Yangsan Fault suggest that the fault appears to be stable, with blocks on both sides of the fault moving in the same direction and at the same displacement rate (Kim and Bae, 2023). Paleoseismic studies on the Korean Peninsula since the 1990s revealed that the most Quaternary surface ruptures were propagated along major structures in the southeastern part of the peninsula, such as the Yangsan Fault, Ulsan Fault, and Yeonil

100 Tectonic Line (Figs. 1b and 1c; Kee et al., 2009; Kim et al., 2011; Choi et al., 2012; Kim et al., 2016). Since the 2016 Gyeongju earthquake, the Yangsan Fault has drawn increasing ~~research~~-attention in various fields, including tectonic geomorphology (Lee et al., 2019; Park and Lee, 2018; Kim and Oh, 2019; Kim et al., 2020d; Kim and Seong, 2021; Hong et al., 2021), ~~fault structure in outcrop- and micro-scale~~~~structural geology~~ (Woo et al., 2015; Choi et al., 2017; Cheon et al., 2017, 2019, 2020a; Kim et al., 2017a, b, 2020a, 2021, 2022; Ryoo and Cheon, 2019; Kwon et al., 2020), paleoseismology (Lee et al., 2015; Choi

105 et al., 2019; Cheon et al., 2020b; Ko et al., 2020; Kim et al., 2023), and fault chronography (Yang and Lee, 2012, 2014; Song et al., 2016, 2019; Sim et al., 2017; Kim and Lee, 2020, 2023). Notably, there are many records of Quaternary surface rupturing with dextral kinematics, which were reactivated along the pre-existing mature (long-lived) Yangsan fault zone (Cheon et al., 2020a). This fault extends  $> 200$  km on land and is several hundred meters wide, with a prevailing horizontal displacement of  $> 20$  km (Choi et al., 2017; Cheon et al., 2017, 2019, 2020a, b). It underwent multiple stages of deformation with various

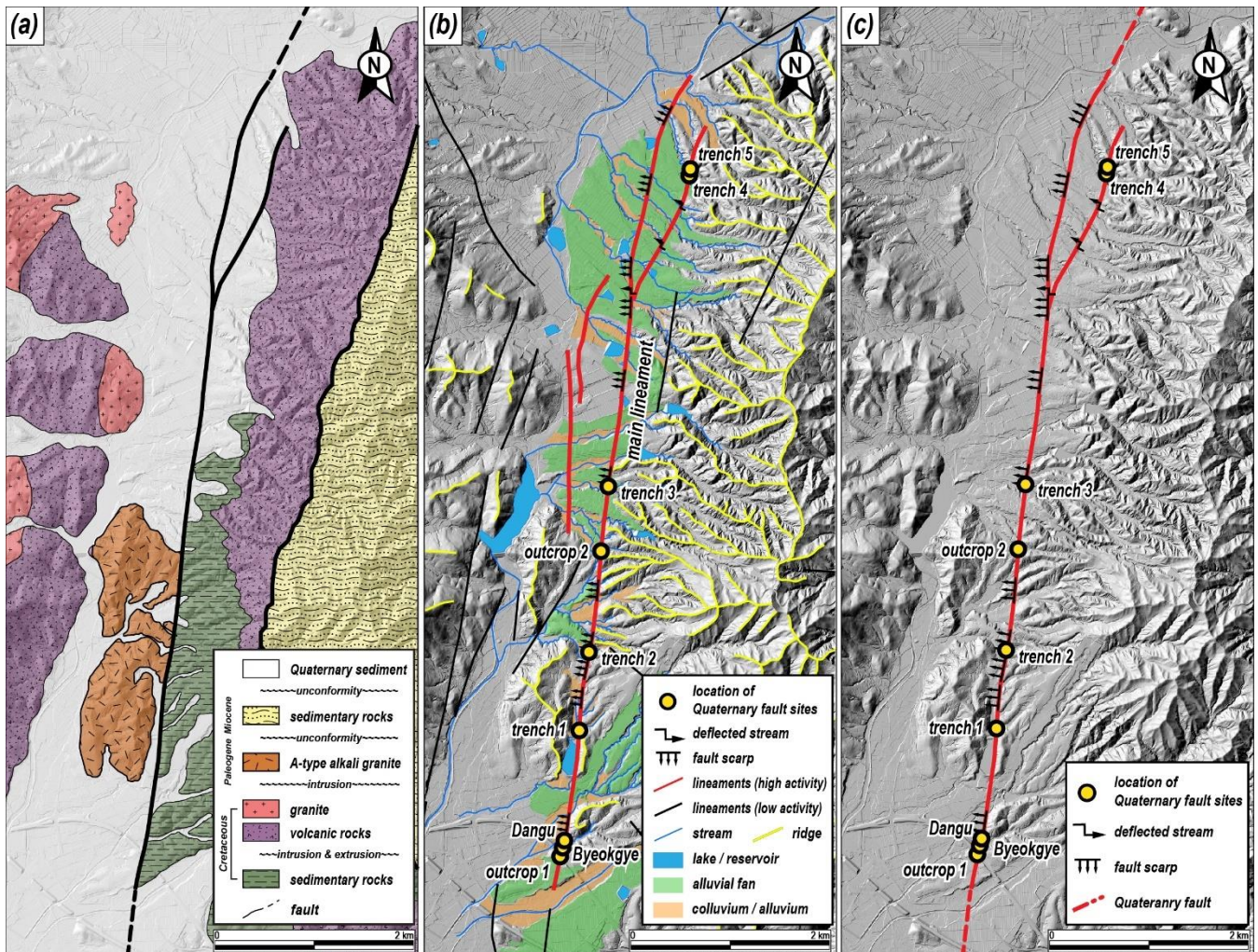
110 kinematic senses during the Cretaceous to Cenozoic (Fig. 1b; Chang et al., 1990; Kim, 1992; Chang and Chang, 1998; Chang, 2002; Hwang et al., 2004, 2007a, b; Choi et al., 2009; Cheon et al., 2017, 2019). The dextral horizontal displacement of the fault is approximately 25–35 km in the Cretaceous sedimentary rocks (Chang et al., 1990) and 21.3 km in A-type alkali granite on both sides of the fault (Fig. 1b; Hwang et al., 2004, 2007a, b).

## 115 2.2 Geological settings of the Byeokgye section of the Yangsan Fault

The Northern Yangsan Fault, located north of Gyeongju at the junction of, the Ulsan and Yangsan faults, has documented several Quaternary surface ruptures (Fig. 1b). These surface ruptures caused offsets in alluvial fans, river terraces, and deflected rivers with dextral displacements of 0.43–2.82 km (Kyung, 2003; Choi et al., 2012; Lee et al., 2019; Han et al., 2021; Ko et al., 2022; Lee et al., 2022; Lee, 2023). Recent ~~significant~~ earthquakes in Pohang and Gyeongju further underscore the seismic activity of this region. The Byeokgye section, which crosses Gyeongju and Pohang, is located in the southern part of the Northern Yangsan Fault, adjacent to the Yugye and Bangok sites to the north (Fig. 1c). In contrast, no Quaternary surface rupture has been identified in the Angang area to the south.

The rocks in the study area are composed of Cretaceous sedimentary, volcanic, and granitic rocks, Paleogene A-type alkaline granite, Middle Miocene sedimentary rocks, and Quaternary sediments (Fig. 2a). The A-type alkaline granite, used as a dextral offset marker for the Yangsan Fault, is distributed on the west side of the fault in the center of the study area and on the east side in Gyeongju and the offset is 21.3 km (Fig. 1b, Hwang et al., 2004, 2007a, b). The Middle Miocene sedimentary rocks in the eastern part of the study area are bounded by the western marginal faults of the Miocene Pohang Basin consisting of normal faults and dextral transfer faults (Fig. 2a; Son et al., 2015; Song, 2015). The Quaternary sediments in the study area are widely distributed along streams and valleys, and stratigraphic features cut by Quaternary surface rupturing along the Yangsan Fault are observed in some places (Fig. 2b, 2c).

In the study area, the Byeokgye (outcrop) and Dangu (trench) sites have been reported as the records of the Quaternary surface ruptures (Fig. 2; Ryoo et al., 1999; Kee et al., 2009; Choi et al., 2012; Lee et al., 2015). The NNE-striking fault splay identified at the Byeokgye site cut the Cretaceous felsic dike and Quaternary sediment. Based on the shear bands within the fault gouge, drag folds in the footwall, and sub-horizontal striations, it was interpreted that strike-slip occurred after reverse slip during the Quaternary (Ryoo et al., 1999). The most recent earthquake (MRE) of the Byeokgye site occurred after  $75\pm 3$  ka, the optically stimulated luminescence (OSL) age of the truncated Quaternary sediments (Choi et al., 2012). The surface ruptures (N10–20°E/75–79°SE) of the two trenches at the Dangu site have geometric and kinematic features similar to those at the Byeokgye site (Lee et al., 2015). The drag fold, slickenline, and three fault gouge zones observed in the exposed walls indicate that at least three strike-slip events with reverse slip occurred after the deposition of Quaternary sediments. In addition, the MRE of the Dangu site using OSL dating, radiocarbon, and archaeological interpretation of artefacts in the Quaternary sediments is  $7.5\pm 3$  ka (Lee et al., 2015). Recently, Song et al. (2020) excavated a trench 1 km north of the Byeokgye site to identify further records on the Quaternary surface rupturing and attempted paleoseismic interpretation. We set this trench as Trench 1 for a comprehensive interpretation and summarize the results.



145 **Figure 2: Detailed study area maps. (a) Geological map of the study area (modified from Hwang et al., 2007; Song, 2015). The A-type alkali granite in the study area is used as a marker of YF's dextral offset. (b) Geomorphological map of the study area (modified from Ha et al., 2022). A fault trace is recognized as an array of fault scarps and deflected streams. (c) Fault trace map of the study area. Two outcrops and five trenches are located in the fault trace.**

### 3 Method

#### 150 3.1 Fault surface rupture tracking and trench siting

Ha et al. (2022) reported a 7.6 km fault trace in the study area through detailed topographic analysis using high-resolution ( $\ll 20$  cm) LiDAR images (Fig. 2b). They interpreted the main lineament as a fault scarp with a vertical displacement of 2–4 m and a dextral refraction channel with a horizontal displacement of 50–150 m. In the trench (Trench 1) on the fault trace, the surface rupture cuts through Quaternary sediments. The detailed topography of the study area is described in Appendix A. We

155 conducted fieldwork along this fault trace, trenched it at four further sites, and identified two natural exposures (described in Appendix C).

### 3.2 ~~Dating methods~~Numerical dating

#### 3.2.1 Quartz OSL and K-feldspar IRSL dating

160 For luminescence dating, a total of thirty-six samples were collected from the five trench walls by inserting light-tight stainless-steel pipes (30 cm long and 5 cm diameter) into sand-rich layers. The sediment samples were then brought into a subdued darkroom to extract pure quartz and K-feldspar grains. The size fractions of 90–250  $\mu\text{m}$  were first separated by wet sieving. Subsequently, these fractions were treated with 10% HCl (~ 1 h) and 10% H<sub>2</sub>O<sub>2</sub> (~ 3 h) to remove carbonates and interstitial organic matter. This was followed by density separation using SPT (sodium polytungstate;  $\rho=2.61 \text{ g/cm}^3$ ). Pure quartz and K-feldspar extracts were finally prepared by etching the sinking (quartz-rich) and floating (K-feldspar-rich) portions with ~ 40 %  
165 and 10% HF (~ 1 h), respectively. The extracts were then rinsed with 10% HCl to dissolve any fluoride precipitates that may have formed during HF etching. The purity of quartz extracts (i.e., the absence of K-feldspar contamination) was determined by comparing infrared-stimulated luminescence (IRSL) and blue-stimulated luminescence (BSL) signals using three natural and beta-irradiated (20 Gy) aliquots. For all quartz extracts, the IRSL signals were negligible, with IRSL to BSL ratios well below 2 %, indicating that K-feldspar grains were effectively removed through the sample preparation procedure.

170 The luminescence signals were measured using a conventional Risø reader (Model TL/OSL-DA-20) installed at the Korea Basic Science Institute (KBSI). The stimulation light sources were Blue-LEDs (470 nm, FWHM 20 nm) for quartz and IR-LEDs (870 nm, FWHM 40 nm) for K-feldspar. The reader was equipped with a 90Sr/90Y source to deliver beta doses to the sample position at a calibrated dose rate of  $0.150 \pm 0.002 \text{ Gy/s}$  (Hansen et al., 2015). The signals were detected through a UV filter (U-340) for quartz OSL and a blue filter pack (a combination of 4 mm Corning 7–59 and 2 mm Schott BG 39) for K-feldspar IRSL.  
175

Quartz OSL equivalent dose ( $D_e$ ) values were estimated using the single-aliquot regenerative-dose (SAR) procedure (Murray and Wintle, 2000), with preheat conditions for main regeneration and test doses of 260°C for 10 s and 220°C for 0 s, respectively. Quartz OSL signals in dose saturation (i.e., for samples older than datable age ranges of quartz OSL dating method) and K-feldspar post-IR IRSL signals, which are well known to have higher dose saturation levels than quartz OSL  
180 (Buylaert et al., 2012), were used as samples for  $D_e$  estimation. K-feldspar post-IR IRSL  $D_e$  values were estimated using the SAR procedure suggested by Buylaert et al. (2009) where, after preheating at 250°C for 60 s, IRSL signals in K-feldspar were read at 225°C for 100 s, immediately followed by lower temperature (50°C) IR stimulation (Hereafter, this signal is referred to as pIRIR<sub>225</sub>). The measured fading rates ( $g_{2\text{days}}$ ) of the K-feldspar pIRIR<sub>225</sub> signals ranged from 0–2 %/dec and fading corrections were made using the R package ‘Luminescence’ (Calc\_FadingCorr; Kreutzer, 2023) to derive the final pIRIR<sub>225</sub>  
185 age estimates. The quartz OSL and fading-corrected K-feldspar pIRIR<sub>225</sub> ages are summarized in Table 2.



### 3.2.2 Radiocarbon dating

Radiocarbon dating was performed to obtain independent ages and to cross-validate the ages of the sediments. Eight charcoal samples are collected from sediment profiles of trenches 1, 2, and 4 and analyzed using accelerator mass spectrometry at the Beta Analytic Radiocarbon Dating Laboratory. The  $^{14}\text{C}$  age was calibrated to calendar years using the OxCal 4.3 (Bronk  
190 Ramsey, 2017) and IntCal 20 (Reimer et al., 2020) atmospheric curves.

### 3.2.3 $^{10}\text{Be}$ - $^{26}\text{Al}$ isochron burial dating

Isochron-burial dating is a variation of conventional burial dating methods that constrains the time elapsed since the sediment burial and has been widely used for dating the alluvial sediments of 5.0–0.2 Ma (Granger & Muzikar, 2001). The burial duration was calculated from the difference between the initial  $^{26}\text{Al}/^{10}\text{Be}$  ratio at the time of burial and the measured ratio of  
195  $^{26}\text{Al}/^{10}\text{Be}$  (Balco & Rovey, 2008; Erlanger et al., 2012). Unlike traditional simple burial dating, which assumes that the initial ratio is known or the same as the surface production ratio of 6.8, isochron-burial dating requires multiple samples with their pre-burial histories (i.e., various initial ratios of  $^{26}\text{Al}/^{10}\text{Be}$ ) to construct an isochron. The initial ratio of  $^{26}\text{Al}/^{10}\text{Be}$  of the samples at burial depended on the erosion and production rates in the source basin. Thus, we assumed that all the analyzed samples originated from the same basin under steady-state erosion. The pre-burial (i.e., inherited) concentrations of the gravel at the  
200 time of burial accumulated with a surface production ratio of 6.8 so that it falls on a line in the plot of  $^{26}\text{Al}$ - $^{10}\text{Be}$  (Lal, 1991; Granger, 2006; Balco and Rovey, 2008). We used the conventional value of 6.8 for the surface production ratio of  $^{26}\text{Al}/^{10}\text{Be}$  for the current study, which can vary depending on longitude, latitude, and altitude (Balco and Rovey, 2008). Without considering the pre-burial exposure history, the measured nuclide concentrations of gravels at the same depth should fall again on a line in the plot of  $^{26}\text{Al}$ - $^{10}\text{Be}$  with a mean life ( $\tau_{pb} = (1/(\lambda_{26} - \lambda_{10}))$ ;  $\sim 2.07$  Ma) because they have the same post-burial  
205 production of  $^{26}\text{Al}$  ( $C_{26}$ ) and  $^{10}\text{Be}$  ( $C_{10}$ ). Thus, the post-burial component can be treated as a constant so that it can be modeled, and the initial ratio of  $^{26}\text{Al}/^{10}\text{Be}$  ( $R_{inh}$ ) can be calculated as

$$N_{26} = (N_{10}R_{inh}e^{-t/\tau_{pb}} + C_{10}R_{inh}e^{t/\tau_{pb}} + C_{26}) \quad (1)$$

The final time ( $t_b$ ) elapsed since burial can be calculated from the decay of the initial isochron ( $R_{inh}$ ) to the isochron of the measured samples ( $R_m$ ):

$$210 \quad t_b = \tau_{pb} \ln(R_m/R_{inh}) \quad (2)$$

### 3.2.4 ESR dating

Electron Spin Resonance (ESR) dating of fault rocks is a method used to derive the timing of faulting by measuring the ESR signal in the quartz of a fault gouge (Ikeya et al., 1982; Lee & Schwarcz, 1994). In general, ESR dating has an age detection limit of up to several thousands of ka (e.g., Lee and Yang, 2003) and is thus helpful for direct dating the timing of faulting.  
215 The ESR signal of quartz grains can be reset when the fault surface is subjected to normal stress of more than 3 MPa and displacements of more than 0.3 m (Kim and Lee, 2020, 2023). These conditions are usually easier to meet at a depth of more

than ~100 m than at the surface. Therefore, it is likely that ESR signals from fault gouges currently exposed at the surface are reset at depths and then brought up to the surface (i.e., current position) via uplift. In addition, in the case that the ESR signals are not completely reset during faulting, the ESR ages may indicate the maximum age of MRE. In our study, we use the ESR ages of samples from trenches and fault sites in the study area reported by Kim and Lee (2023) to estimate the number of earthquakes.

### 3.3 Paleo-stress reconstruction

Paleo-stress reconstruction of Quaternary rupturing was carried out using 20 slickenlines obtained from five trenches. The data were analyzed using Wintensor S/W (v.5.8.5; Delvaux and Sperner, 2003). The type of stress regime is expressed quantitatively using the R' value:  $R' = R$  ( $\sigma_1$  is vertical), or  $2-R$  ( $\sigma_2$  is vertical), or  $2+R$  ( $\sigma_3$  is vertical);  $R = (\sigma_2 - \sigma_3) / (\sigma_1 - \sigma_3)$  (Delvaux et al., 1997).

### 3.4 Displacement and earthquake magnitude estimation

The slickenlines of the main surface rupture and the vertical separation of the Quaternary sediments in the trench wall are used to determine the horizontal displacement of the MRE and the displacement per event. In general, for strike-slip faults like the study area, horizontal displacements must be obtained from 3D trenches or from topography that preserves the displacements almost intact (e.g., Kim et al., 2024; Naik et al., 2024). Using only 2D trenches to obtain displacements or slip rates is uncertain because the sedimentary layers are unlikely to have recorded all earthquakes. Furthermore, deriving the horizontal displacement is challenging when exposed walls are inclined, markers are inclined, or the slip sense is not purely dip-slip or strike-slip (which is almost always the case). In addition, displacements based on fragmentary information, such as bedrock separation and thickness of Quaternary sediments, can be over- or underestimated by fault slip motion and the possibility of paleo-topographic relief cannot be ignored. Despite these uncertainties, fault displacement is a necessary factor in earthquake magnitude estimation and key paleoseismological information, and the displacement obtained from the 2D trench can be used as a minimum value; therefore, the process of collecting or estimating fault displacement is indispensable in paleoseismology. Therefore, correlations based on vertical separation, marker dip angle, angle of slope wall, fault dip angle, rake of slickenline, etc. are important for estimating the horizontal displacement of a fault (Fig. B1; Xu et al., 2009; Jin et al., 2013; Lee et al., 2017; Gwon et al., 2021). The method of using their relationship to find the horizontal displacement is described in detail in Appendix B.

Variables used for earthquake magnitude estimation include average displacement (Kanamori, 1977), maximum displacement (MD; Bonilla et al., 1984; Wells and Coppersmith, 1994), surface rupture length (Bonilla et al., 1984; Khromovskikh, 1989; Wells and Coppersmith, 1994), rupture area (Wells and Coppersmith, 1994), and surface rupture length  $\times$  MD (Bonilla et al., 1984; Mason, 1996). However, in Korea, where rupture traces are difficult to find, it is difficult to use surface rupture length or rupture area owing to large uncertainties. Thus, we used MD (horizontal displacement), which is relatively easy to obtain from outcrops and trenches and more reliable. Many previous studies within intraplate have applied the empirical relationship of the MD-moment magnitude ( $M_w$ ) presented by Wells and Coppersmith (1994) (e.g., Patyniak et al., 2017 in Kyrgyzstan;

Suzuki et al., 2021 in Mongolia; Ge et al., 2024., in China). We also estimated the maximum earthquake magnitude by applying the MD obtained from the trench to the empirical formula. The rake of slickenlines on the Quaternary slip surface that underwent faulting averages  $20^\circ$  and strike-slip motion is dominant; therefore, we used a corresponding strike-slip fault type  $M_w$ -MD empirical relationship.

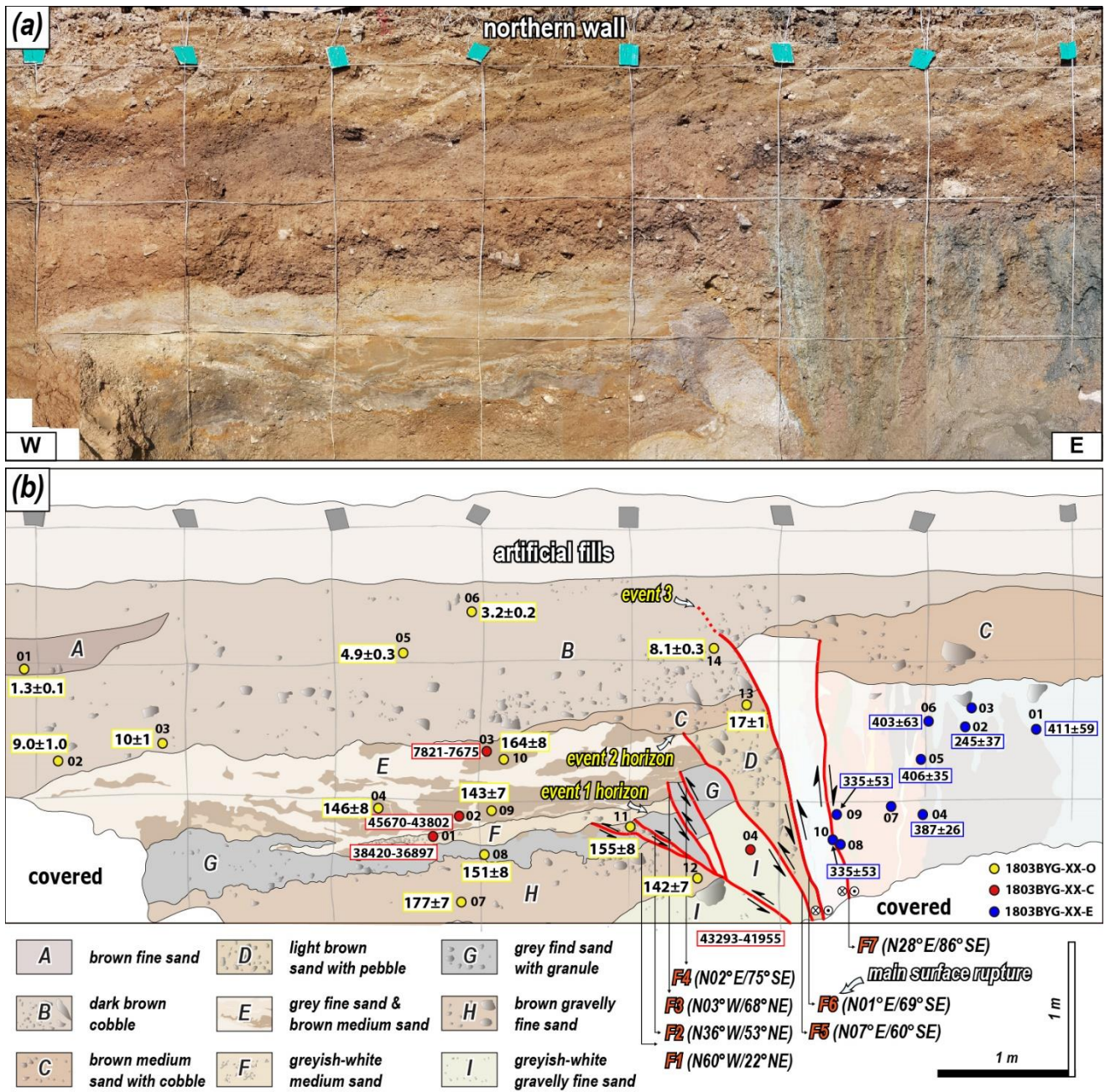
## 4 Results

### 4.1 Characteristics of Quaternary faulting in the trench

#### 4.1.1 Trench 1

Trench 1, previously reported by Song et al. (2020) and Ha et al. (2022), is summarized as follows: It is located on the main lineament, approximately 1 km north of the Byeokgye site (Fig. 2c), within a cultivated field where a narrow 50 m wide N-S trending valley and a 20 m wide NE-trending valley meet, through which the main lineament passes. To the east of Trench 1, a NE-trending ridge develops, although this is currently difficult to identify due to human modification, while to the west, a hill with a N-S trending ridge is formed (Fig. A2). Fault scarps are distinctly visible along the main lineament, both to the south and north of Trench 1, with small fluvial and colluvial deposits observed on the surface. Nine Quaternary sedimentary units and seven east-dipping splay slip surfaces (F1–F7) cutting the units are found in the E-W trending trench wall (Fig. 3). The hanging wall of F6 is the western boundary of pre-existing fault core more than 2.5 m wide and the footwall of F6 is a 4 m thick Quaternary sedimentary unit overlying the A-type alkali granite. The pre-existing fault core is divided into two zones based on whether it is related to rupturing. Between F6 and F7, the fault core had a 40 cm wide blue fault gouge cutting Quaternary sediments and a weakly developed shear band within the fault gouge. The fault core, eastern side of F7, did not cut the Quaternary sediments and consisted of a brown to dark grey brecciated zone and a gouge zone more than 2 m wide. The stratigraphic features of the nine units are listed in Table 1, and there are two noteworthy observations: First, the triangular-shaped unit D, characterized by a light brown sandy matrix with better sorting and roundness compared to the surrounding units, is surrounded by the slip surfaces (Fig. 3). It indicates that unit D may have been captured by the horizontal displacement of nearby sediments during the faulting event. Second, various types of seismogenic soft-sediment deformation structures (SSDs) are developed in units E and G (Fig. 3, Fig. 10 in Ha et al., 2022). The orientations of slip surfaces ranged from  $N60^\circ W$  to  $N28^\circ E$ , changing from NW-to NE-striking to the east. The F6 fault splay ( $N01^\circ E/69^\circ SE$ ) cut through unit B and the F7 splay ( $N28^\circ E/86^\circ SE$ ) is terminated in unit C. F3, F4 and F5 cut through units D, E, and F, respectively, and are terminated under unit C. F1 and F2 cut through units G, H, and I but not through unit F. The rakes of the slickenline observed on F6 measured  $15\text{--}55^\circ$ , indicating a dextral slip with a reverse component. Three faulting events are interpreted based on the geometry of the sediments and the kinematics of the slip surface: (1) The first faulting event involves the rupture of all F1-F7 after the deposition of units G, H, and I before the deposition of unit F, marking the event 1 horizon. (2) The second faulting event occurred after the deposition of units E and F prior to the deposition of unit C, defining the event

280 2 horizon, with ruptures affecting faults F3 through F7. During this event, dextral slip along faults F5 and F6 displaced unit D.  
(3) The third faulting event took place after the deposition of units B and C, with rupture limited to faults F6 and F7.  
OSL/pIRIR<sub>225</sub> ages are presented in Table 1. We also conducted <sup>14</sup>C and ESR dating on the trench. Three charcoal samples  
(1803BYG-01-C, 1803BYG-02-C, and 1803BYG-03-C) were collected from unit E and one charcoal sample (1803BYG-04-  
285 36,897 and 45,670–43,802 Cal yr BP, respectively (Table 2). However, the ages of these two samples are near the upper limit  
of the radiocarbon dates and are stratigraphically contradictory, with the lower layer being younger than the upper layer. The  
age of 1803BYG-03-C (7,821–7,675 cal yr BP) from the upper part of unit E is inconsistent with the OSL age (1803BYG-10-  
O: ~164 ka). It is possible that liquefaction in unit E caused a disturbance in the sediments and that the radiocarbon and OSL  
dates do not indicate the exact depositional timing. In addition, the radiocarbon age of 43,292–41,955 cal yr BP for the sample  
290 from unit I is near the upper limit of the radiocarbon ages and is thus subject to error. In particular, it is younger than K-feldspar  
pIRIR<sub>225</sub> (177±7 ka (1803BYG-07-O)) from unit H, making it unlikely that this age is indicative of the depositional age of unit  
I. The main surface rupture cut unit B and the MRE using the OSL age of unit B is <3.2±0.2 ka (1803BYG-06-O; Table 1, Fig.  
3). The geometry and cross-cutting relationship between the Quaternary sediments and the seven surface ruptures indicated  
that a pre-existing fault core is reactivated during the Quaternary, resulting in at least three faulting events (Fig.3; Fig. 9 in  
295 Song et al., 2020): the first (antepenultimate earthquake, AE) occurring at <142±4 ka (1803BYG-12-O), the second  
(penultimate earthquake, PE) at >17±1 ka (1803BYG-13-O), and the third at the MRE (Table 1, Fig. 3). For ESR dating, 36  
fault gouge samples were collected from eastern side of F7, and ESR dating is performed on 10 of them (1810BYG-01 to 10-  
E) (Fig. 3). The dates of each sample are presented in Table 3. The weighted average ESR ages of the samples from the same  
fault viscose band are 245±37 ka (1810BYG-02-E, 1810BYG-10-E), 406±35 ka (1810BYG-01-E, 1810BYG-05-E, 1810BYG-  
300 06-E), 387±26 ka (1810BYG-04-E), and 335±53 ka (1810BYG-04-E) (Table 3). Samples with dose-saturated ESR signals  
(1810BYG-03-E, -07-E, and -08-E) are excluded from the weighted average age calculations. Considering the error, the timing  
of faulting events using ESR ages at these sites can be determined to be 406±35 and 245±37 ka.



305

Figure 3: (a) Photomosaic of the trench 1 wall of the northern wall. The colored circles represent samples for age dating. (b) Detailed sketch of the trench 1 exposed wall. Light grey lines indicate a 1 × 1 m grid. The numbers in the yellow, red, and blue boxes represent OSL and IRSL (ka), radiocarbon (cal yr BP), and ESR (ka) dating results, respectively.

**Table 1. Description and OSL/pIRIR<sub>225</sub> dating results of the units in each trench**

| Unit            | Features   | Age       |                      |               |
|-----------------|--|-----------|----------------------|---------------|
|                 |  | Age (ka)  | Dating method        | Sample number |
| <b>Trench 1</b> |  |           |                      |               |
| A               | Brown fine sand, lens shape in unit B, coarsening upward in the bottom (silt to fine sand)   | 1.3 ± 0.1 | OSL                  | 01            |
|                 |  | 9.0 ± 1.0 | OSL                  | 02            |
| B               | Dark brown cobble, fine sand matrix, poor roundness, fining upward in clast (cobble to pebble) and matrix (sand to fine sand), the youngest unit cut by rupture  | 10 ± 1    | OSL                  | 03            |
|                 |  | 4.9 ± 0.3 | OSL                  | 05            |
|                 |  | 3.2 ± 0.2 | OSL                  | 06            |
|                 |  | 8.1 ± 0.3 | OSL                  | 14            |
| C               | Brown medium sand with cobble, good roundness and sorting compared to unit b, pinch out in footwall, cover the pre-existing fault core   | 17 ± 1    | OSL                  | 13            |
| D               | Light brown sand with pebble, good roundness and sorting despite adjacent rupture, captured by a triangular shape, with ruptures   | -         | -                    | -             |
| E               | Grey fine sand and brown medium sand, mixing with grey and brown parts, SSDS (load structure dominated; load cats, pillar structure, sand dike, disturbed structure, structureless sediments)                    | 146 ± 8   | pIRIR <sub>225</sub> | 04            |
|                 |  | 143 ± 7   | pIRIR <sub>225</sub> | 09            |
|                 |  | 164 ± 8   | pIRIR <sub>225</sub> | 10            |
| F               | Greyish-white medium sand  | -         | -                    | -             |
| G               | Grey fine sand with granule, SSDS (intrusive structure dominated; ball and pillow, flame structure, sand dike)   | 151 ± 8   | pIRIR <sub>225</sub> | 08            |
|                 |  | 155 ± 8   | pIRIR <sub>225</sub> | 11            |
| H               | Brown gravelly fine sand, moderate roundness and sorting   | 177 ± 7   | pIRIR <sub>225</sub> | 07            |
|                 |  | 142 ± 7   | pIRIR <sub>225</sub> | 12            |
| I               | Greyish-white gravelly fine sand, matrix derived from granite that basement rock   | -         | -                    | -             |
| <b>Trench 2</b> |  |           |                      |               |
| A               | Reddish brown cobble deposits, A subangular clast composed of granitic and sedimentary rocks with a maximum diameter of 40 cm, poor sorting, charcoal in the bottom, cover the pre-existing fault core           | 3.2 ± 0.3 | OSL                  | 05            |
|                 |  | 3.4 ± 0.4 | OSL                  | 06            |
|                 |  | 19 ± 1    | OSL                  | 07            |
| B               | Light grey silt-light yellowish brown fine sand, interbedded two layers, cut by surface rupture  | -         | -                    | -             |
| <b>Trench 3</b> |  |           |                      |               |
| A               | Dark brown fine sand-silt  | -         | -                    | -             |
| B               | Light brown boulder-cobble deposits, colluvial deposits from mountain slopes, moderate roundness, decreasing the clast size toward the west, cover the Quaternary slip zone                                      | 6.4 ± 0.4 | OSL                  | 10            |
| C               | Brown pebble deposits, poor roundness and sorting, brown sand matrix, the youngest unit cut by fault splays  | -         | -                    | -             |
| D               | Yellowish-brown pebble deposits, colluvial wedge, triangular shaped, angular to subangular clast, poor sorting in bottom, fining upward, sand content increases with distance from the main Quaternary slip zone | 137 ± 3   | pIRIR <sub>225</sub> | 08            |
| E               | Brown cobble-pebble deposits, subangular clast, poor sorting, intercalated fine sand to silt   | 173 ± 6   | pIRIR <sub>225</sub> | 02            |
|                 |  | 175 ± 5   | pIRIR <sub>225</sub> | 03            |
| F               | Brown sand-fine sand   | -         | -                    | -             |
| G               | Brown pebble deposits, subangular clast, poor sorting, clast composed of granitic, volcanic, sedimentary rocks   | -         | -                    | -             |
| H               | Brown sand-fine sand   | -         | -                    | -             |
| <b>Trench 4</b> |  |           |                      |               |
| A               | Brown fine sand, have a charcoal   | 0.15±0.01 | OSL                  | 07            |
|                 |  | 0.15±0.01 | OSL                  | 08            |
| B               | Dark brown cobble deposits-sand, colluvial deposits from mountain slopes, subangular clast, poor sorting, the youngest unit cut by surface rupture   | 1.3 ± 0.1 | OSL                  | 05            |
|                 |  | 1.2 ± 0.1 | OSL                  | 06            |
|                 |  | 5.9 ± 0.4 | OSL                  | 09            |
| C               | Light brown boulder deposits-sand, matrix is coarse sand to sand, angular clast, poor sorting, clast mainly composed of granite, the maximum diameter of a clast is ~ 120 cm                                     | -         | -                    | -             |
| D               | Brown sand-fine sand, fining upward  | -         | -                    | -             |
| E               | Brown cobble deposits-coarse sand, alternating sand and gravel, average diameter of clast is 2–5 cm, subangular to angular, moderate sorting   | -         | -                    | -             |
| F               | Light brown sand-fine sand   | -         | -                    | -             |
| <b>Trench 5</b> |  |           |                      |               |
| A               | Reddish brown pebble deposits, A subangular clast composed of granitic, sedimentary, volcanic rocks with a maximum diameter of 15 cm, good sorting, matrix-supported   | -         | -                    | -             |
| B               | Reddish brown fine sand-silt, weak horizontal bedding, the youngest unit cut by surface rupture, no truncation or deformation after MRE.   | 2.8 ± 0.1 | OSL                  | 03            |
|                 |  | 2.6 ± 0.1 | OSL                  | 04            |
| C               | Reddish brown cobble-pebble deposits, fine sand matrix, clast composed of granitic, sedimentary, volcanic rocks, angular to sub-angular clast, poor sorting, containing clasts almost 40%.                       | 10 ± 1    | OSL                  | 01            |
|                 |  | 4.8 ± 0.2 | OSL                  | 02            |
| D               | Light bluish-grey pebble deposits, light grey fine sand matrix, the maximum diameter of a clast is ~ 20 cm, clast composed of sedimentary, volcanic rocks, angular to sub-angular clast, poor sorting            | -         | -                    | -             |
| E               | Light yellowish brown pebble deposits, A slit near the rupture gradually increases in grain size as it moves away, changing to a pebble deposit, angular to sub-angular clast, good sorting                      | -         | -                    | -             |

310 **Table 2. <sup>14</sup>C dating results**

| Sample name  | Material dated | $\delta^{13}\text{C}$ (‰) | <sup>14</sup> C age (yr) | Calibrated age (cal yr BP) <sup>a</sup> | Probability (%) <sup>b</sup> |
|--------------|----------------|---------------------------|--------------------------|---|------------------------------|
| 1803BYG-01-C | Charcoal       | -25.1                     | 33,400±220               | 38,420–36,897                           | 95.4                         |
| 1803BYG-02-C | Charcoal       | -27.4                     | 41,250±500               | 45,670–43,802                           | 95.4                         |
| 1803BYG-03-C | Sediment       | -24.7                     | 6,910±30                 | 7,821–7,675                             | 95.4                         |
| 1803BYG-04-C | Charcoal       | Not analyzed              | 38,560±480               | 43,293–41,955                           | 95.4                         |
| 1810NSR-01-C | Charcoal       | -27.8                     | 170±30                   | 291–0                                   | 95.4                         |
| 1810NSR-02-C | Charcoal       | -26.3                     | 210±30                   | 304–0                                   | 95.4                         |
| 2009UGR-01-C | Sediment       | -24.2                     | 25,230±100               | 29,576–28,966                           | 95.4                         |
| 2009UGR-02-C | Charcoal       | -26.9                     | 160±30                   | 286–0                                   | 95.4                         |
| 2009UGR-03-C | Sediment       | -22.5                     | 540±30                   | 634–513                                 | 95.4                         |

<sup>a</sup> Calibration used the database INTCAL13 (Reimer et al., 2013)

<sup>b</sup> Probability Method (Bronk Ramsey, 2009)

**Table 3. ESR dating results (from Kim and Lee, 2023)**

| Trench   | Sample number |        |         |          |        |        |      |      |        |        |
|----------|---------------|--------|---------|----------|--------|--------|------|------|--------|--------|
|          | 01            | 02     | 03      | 04       | 05     | 06     | 07   | 08   | 09     | 10     |
| Byeokgye | 421±27        | 396±24 | 871±63  | 1886±319 |        |        |      |      |        |        |
| Trench 1 | 411±59        | 245±37 | n.d.    | 387±26   | 406±35 | 403±63 | n.d. | n.d. | 335±53 | 248±40 |
| Trench 2 | 790±60        | 409±41 | 405±32  | n.d.     | 369±53 | 330±44 | n.d. | n.d. | 261±48 |        |
| Trench 3 | 425±66        | 409±52 | 702±123 | n.d.     |        |        |      |      |        |        |

315 **n.d. = Not Determined**

**The details of all data are in Kim and Lee (2023)**

#### 4.2.2 Trench 2

Trench 2 is located on the main lineament 0.8 km north of Trench 1 (Fig. 2c), within a colluvial area where fault scarp extend continuously along the main lineament to the south and north. Just north of Trench 2, the transition to an alluvial fan is clearly visible where the mountain ridge meets the main lineament. The 25-m wide valley surface contains partially developed colluvial sediments and deposits from small streams and gullies. Two Quaternary deposits are observed in Trench 2, along a low-angle Quaternary slip surface (N02°E/38°SE) intersecting the Quaternary deposits on the exposed wall (Fig. 4). The minimum 6-m-wide fault core of the hanging wall is composed of mature fault rocks. The fault core is divided into yellow and bluish-grey (Fig. 4). Foliation developed within the yellow fault core, which abutted the Quaternary slip surface in the upper part of the wall. The Quaternary slip surface cuts unit B, displaying thrusting of the hanging wall's pre-existing fault core, while unit A overlies both features. Unit A has a loose matrix and relatively low consolidation compared to the underlying unit B and overlies the pre-existing fault core (Table 1). The slickenline on the Quaternary slip surface shows a dextral slip with a minor reverse component. Only one faulting event is recognized, in which the Quaternary slip surface cuts through unit B, and unit A overlies it (Fig. 5b, 5d).

The OSL ages of unit A, which covers the rupture, are  $3.4\pm 0.4$  ka (1810NSR-06) and  $3.2\pm 0.3$  ka (1810NSR-05) at the southern wall and  $19\pm 1$  ka (1810NSR-07) at the northern wall (Table 1). The radiocarbon ages of the charcoal in unit A are 291–0 and 304–0 cal yr BP (Table 2), making them much younger than the OSL age from unit A. Radiocarbon dates do not indicate when the charcoal is deposited with the sediment but when the tree died after being rooted in the ground. The OSL results indicate a depositional age of  $3.4\pm 0.4$  ka for unit A, which is not cut by the rupture, so the MRE of the surface rupture in Trench 2 is interpreted to be before  $3.4\pm 0.4$  ka. The ESR ages obtained from the fault gouge are higher than the depositional ages of the sediments cut by the rupture (Table 3). The ESR ages suggest that the quartz ESR signal in the fault gouge is not fully initialized during faulting. Nevertheless, the ESR ages roughly cluster into four periods:  $790\pm 60$  ka (1810NSR-01-E),  $407\pm 37$  ka (1810NSR-02, 03-E),  $350\pm 49$  ka (1810NSR-05, 06-E), and  $261\pm 48$  ka (1810NSR-09-E).

To estimate the thickness of the Quaternary sediments and the cumulative vertical displacement of the Quaternary slip, drilled sediments were sampled from the footwall along the Quaternary slip surface (Fig. D1). The Quaternary sediments extend to a depth of approximately 32.8 m, underlain by a granite wash (1.2 m thick) of Paleogene A-type alkali granite, and a subsequent fault damage zone of the granite exists at its base (Fig. D1). Therefore, the vertical separation caused by the Quaternary rupture in Trench 2 is at least 34 m. However, the vertical separation is a paleo-topographic relief difference that may have been caused by the strike-slip movement of the Quaternary slip. Cosmogenic  $^{10}\text{Be}$ - $^{26}\text{Al}$  isochron dating of the granite wash underlying the Quaternary sediments yielded a burial age of  $2,871\pm 593$  ka, indicating that the thick Quaternary sediments started to be deposited after  $2,871\pm 593$  ka (Table 4).



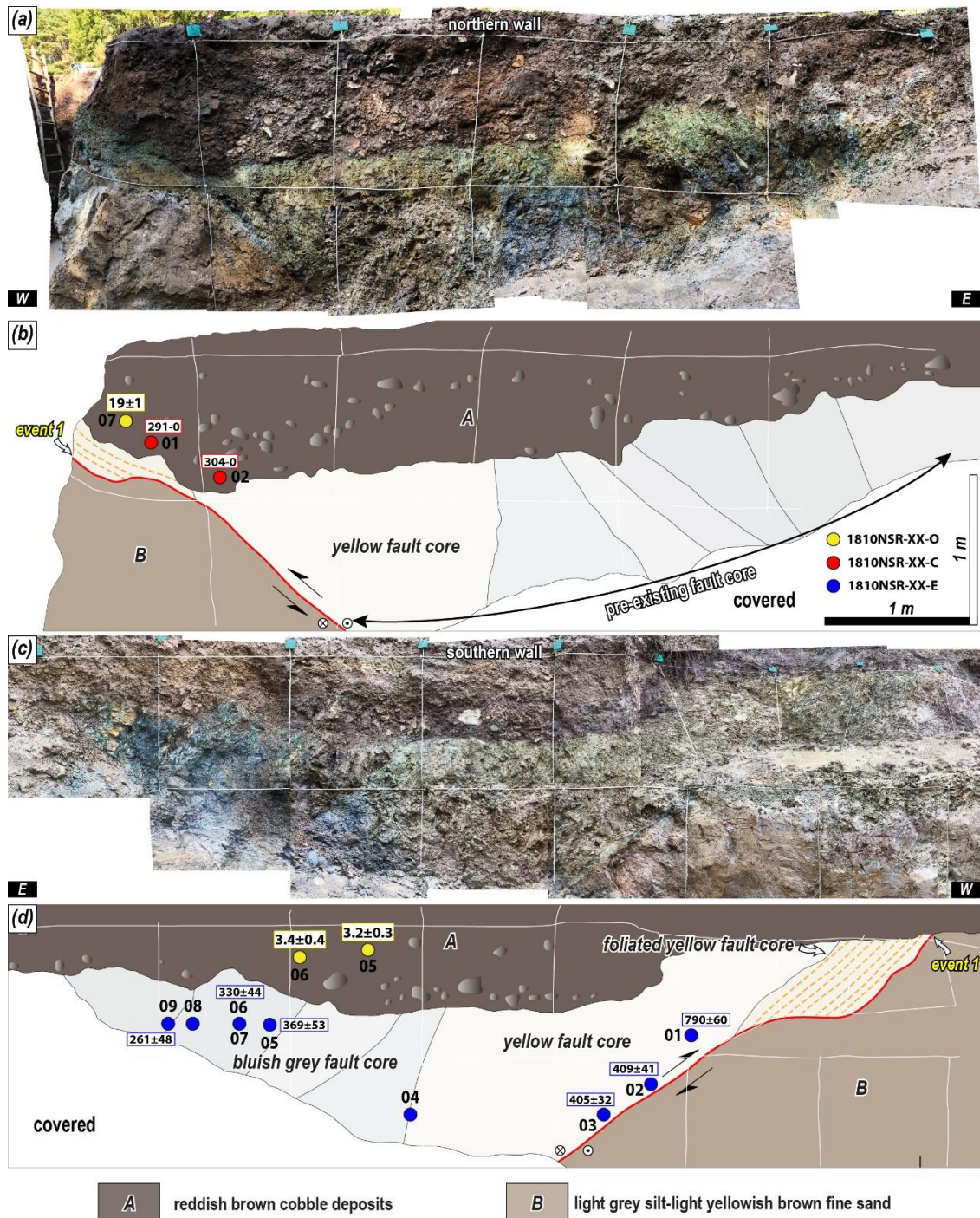


Figure 4: Photomosaic of the trench 2 exposed wall of the (a) northern and (c) southern walls. The colored circles represent samples for age dating. Detailed sketch of the trench 2 exposed wall of the (b) northern wall and (d) southern wall. White lines indicate a 1 m × 1 m grid. The numbers in the yellow, red, and blue boxes represent OSL and IRSL (ka), radiocarbon (cal yr BP), and ESR (ka) dating results, respectively.

350

**Table 4. Cosmogenic  $^{10}\text{Be}$ - $^{26}\text{Al}$  isochron burial dating results of granite wash at Trench 2**

| Name               | Latitude<br>(°N, DD) | Longitude<br>(°E, DD) | Elevation<br>(m asl) | Depth <sup>a</sup><br>(m) | Density <sup>b</sup><br>(g·cm <sup>-3</sup> ) | $^{10}\text{Be}$ Conc.<br>( $10^4$ atoms g <sup>-1</sup> ) | $^{27}\text{Al}$ Conc.<br>( $10^4$ atoms g <sup>-1</sup> ) | $^{26}\text{Al}/^{10}\text{Be}^c$ | Isochron<br>Age <sup>d,e</sup> (Ma) |
|--------------------|----------------------|-----------------------|----------------------|---------------------------|---|--|--|-----------------------------------|-------------------------------------|
| NAN001             | 36.075519            | 129.256658            | 104                  | 28                        | 2.0   | 12.12 ± 0.53   | 23.39 ± 2.16   | 1.93                              |                                     |
| NAN002             | 36.075519            | 129.256658            | 104                  | 28                        | 2.0   | 2.08 ± 0.08  | 6.89 ± 0.83  | 3.31                              |                                     |
| NAN003             | 36.075519            | 129.256658            | 104                  | 28                        | 2.0   | 2.41 ± 0.10  | 10.39 ± 1.08   | 4.30                              |                                     |
| <b>2.87 ± 0.59</b> |                      |                       |                      |                           |   |  |  |                                   |                                     |

<sup>a</sup> Relative depth from the surface.

<sup>b</sup> Density of unconsolidated sediment.

355 <sup>c</sup> Production ratio for the surface is 6.75.

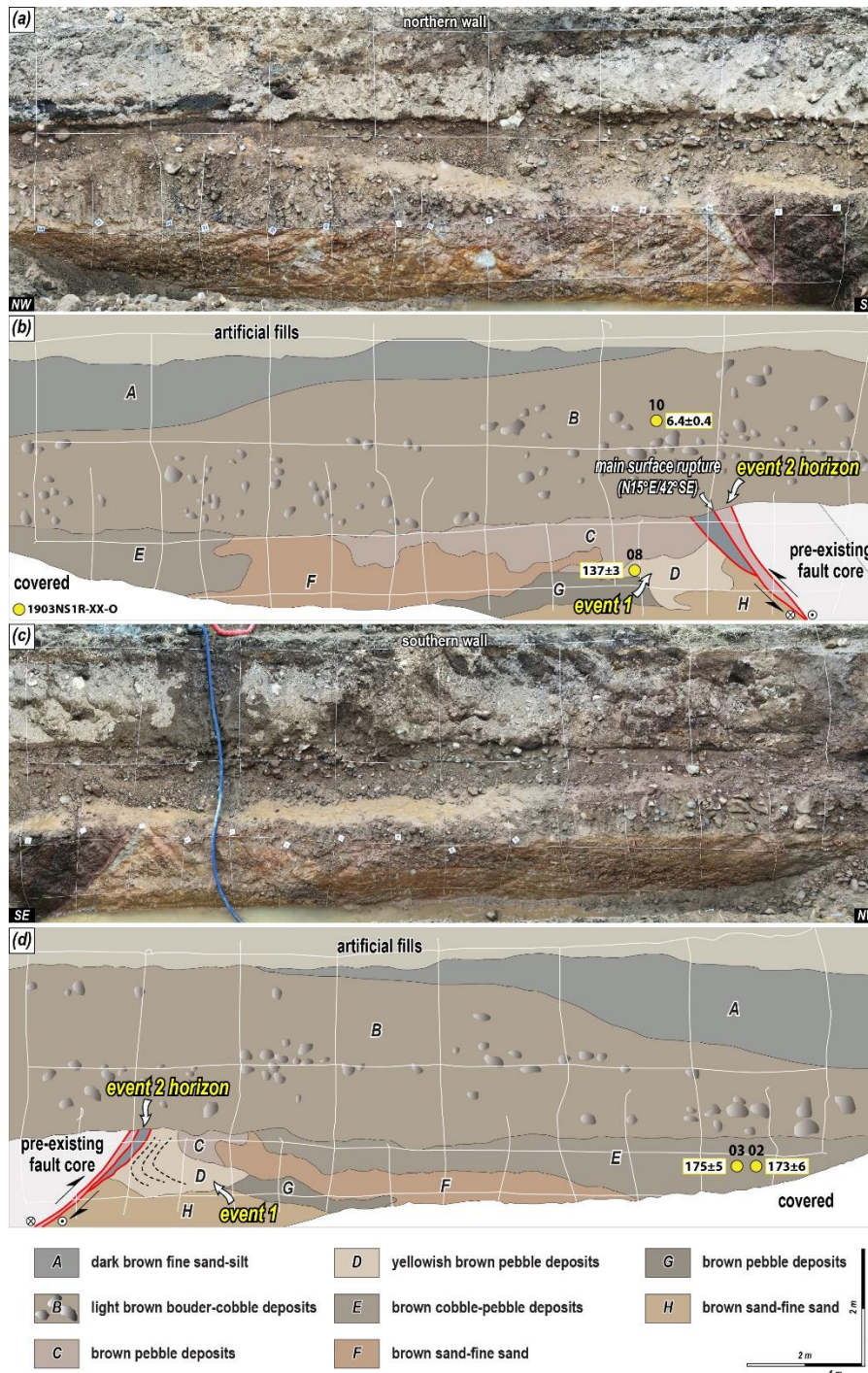
<sup>d</sup> Uncertainties are calculated at the 1 $\sigma$  confidence interval.

<sup>e</sup> All errors are propagated.

### 4.2.3 Trench 3

Trench 3 is located on the main lineament extending 1.7 km north of the Trench 2 (Fig. 2c), within a cultivated field next to a wide road at the mouth of a broad basin. Fault scarps along the main lineament extend both south and north of the Trench 3. This trench marks the northernmost point where the transition to the alluvial fan is observed where the mountain ridge meets the main lineament; beyond this point, fault scarps continue to develop on the alluvial fan surface. Eight Quaternary sedimentary units and three fault splays are identified in the trench wall (Fig. 5, Table 1). The hanging wall of the Quaternary slip zone, which cut through Quaternary sediments, is composed of a pre-existing fault core. Excavation revealed a fault core at least 20 m wide. The fault gouge zone that cut the Quaternary sediments is narrower than 5 cm at the bottom of the wall and widened to 40 cm at the top of the wall; it is divided into a greyish-white gouge zone and a red gouge zone by color and slip surface. The red fault gouge zone is almost entirely composed of clay; however, there are numerous uncrushed quartz and rock fragments within the grayish-white gouge zone. The characteristics of the eight units are shown in Table 1. Unit D is a colluvial wedge that indicates a paleo-earthquake (Fig. 5, Table 1). Brown sand to fine (units F and H) and brown gravel (units C, E, and G) deposits are in the trench wall. These features can be attributed to environmental factors, such as deposition due to repeated rainfall, flooding, or seismic events due to repeated seismic motion. The Quaternary slip zone cuts through unit C, including unit D, a colluvial wedge, and is covered by unit B. The slickenline observed on the fault splays indicates a dextral slip with a small reverse component. There are at least two estimated faulting events in this exposed wall: event 1, which formed a colluvial wedge, and event 2, which cut the colluvial wedge (Fig. 5).

The pIRIR<sub>225</sub> ages of sample 1903NR1R-02 and 03-O from unit E at the southern wall are 173±6 ka and 175±5 ka, respectively. In contrast, the pIRIR<sub>225</sub> age of 1903NR1R-08-O from unit D, which is the colluvial wedge that directly indicates the timing of a faulting event, shows that the deposit formed at 137±3 ka (Table 1). Additionally sample 1903NR1R-10-O from unit B, which covers the rupture, is dated as 6.4±0.4 ka. These findings suggest that the first surface rupture occurred at 137±3 ka, as indicated by the colluvial wedge, and the next surface rupture occurred before 6.4±0.4 ka indicated by event 2 horizon. The youngest ESR age for the fault gouge is 409±52 ka (1903NR1R-02-E, Table 3). However, since the quartz ESR signal in the fault zone may not fully reset during faulting, this age implies that the faulting event occurred at or after 409±52 ka. The ESR ages cluster into two time periods: 417±59 ka (1903NR1R-01, 02-E), 702±123 ka (1903NR1R-03-E).



385

**Figure 5:** Photomosaic of the trench 3 wall of the (a) northern wall and (c) southern wall. The colored circles represent samples for age dating. Detailed sketch of the trench 3 wall of the (b) northern and (d) southern walls. White lines indicate a 1 × 1 m grid. Black dot line reveals bedding trace. The numbers in the yellow, red, and blue boxes represent OSL and IRSL (ka), radiocarbon (cal yr BP), and ESR (ka) dating results, respectively.

#### 4.2.4 Trench 4

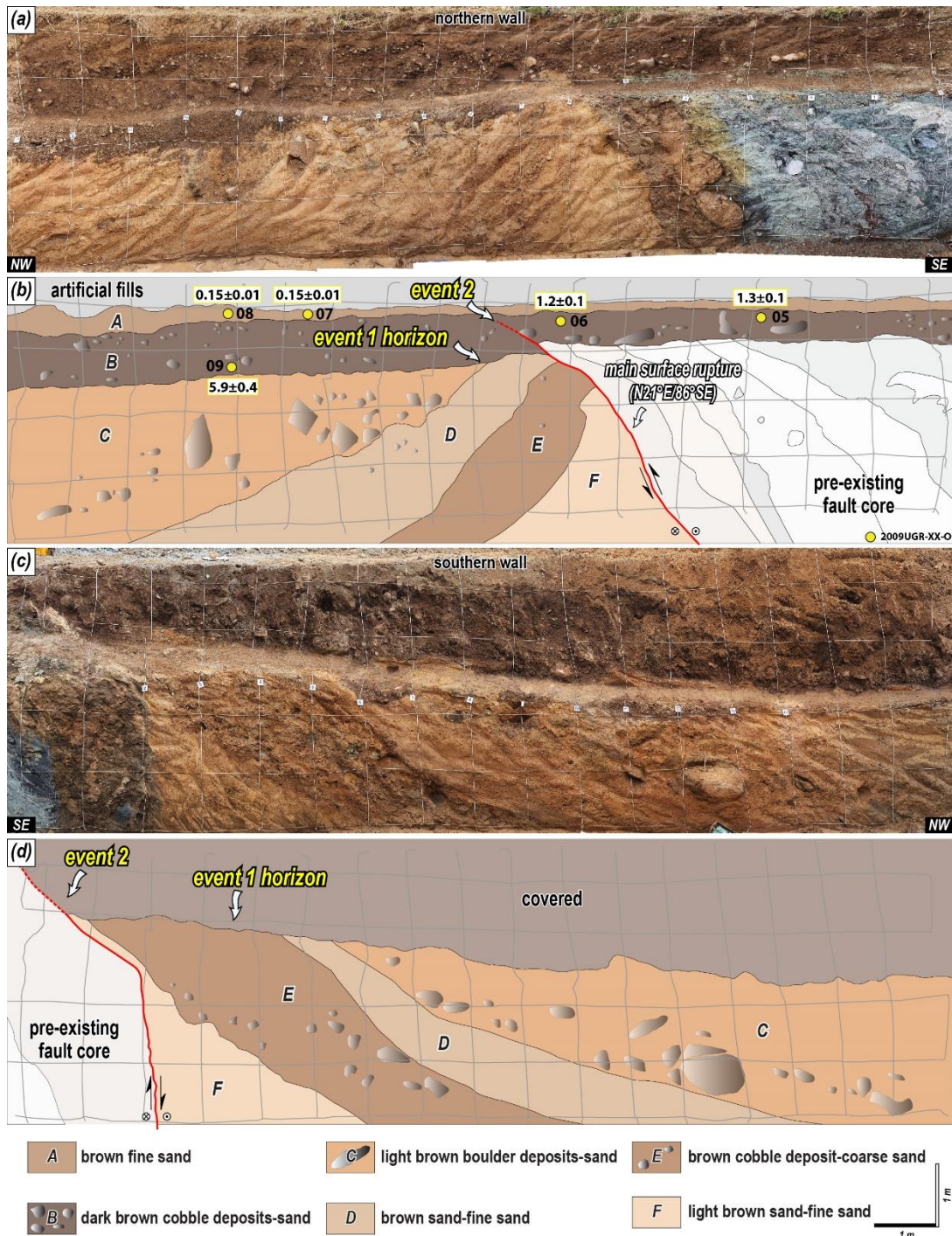
390 Trench 4 is situated on a NE-striking eastern branch lineament from the main lineament, which stretches 2.8 km north of the  
Trench 3 (Fig. 2c). South of Trench 4, three continuous dextrally deflected streams follow the branching lineament, with  
smaller displacements identified further north. Trench 4 lies at the edge of an alluvial fan near a hillslope, with two features  
separated by a stream. Within the trench wall, five Quaternary sedimentary units are cut by a surface rupture (Fig. 6, Table 1).  
The hanging wall of the Quaternary fault splay includes a pre-existing fault core at least 5 meters wide at the time of excavation.

395 Adjacent to the Quaternary sediments, a 20-cm-wide fault gouge zone developed, characterized by yellowish-brown and  
reddish-brown gouges. Units A and B exhibit horizontal to sub-horizontal bedding, while the bedding of units C-F tilts  
westward, with dips of up to  $50^\circ$  near the surface rupture, becoming shallower to the west (Fig. 6, Table 1). The difference in  
bedding orientations indicates an angular unconformity between unit B and units C–F. A surface rupture, covered by unit A,  
cuts through all of units C-F, including the unconformity, but does not extend through all of unit B. The slickenlines observed

400 on the fault splay indicating dextral slip with a minor reverse component. At least two faulting events are inferred from the  
exposed wall: the first faulting event (PE) caused the tilting of units C–F after deposition (event 1 horizon), and MRE occurred  
during the deposition of unit B, following the formation of the angular unconformity (Fig. 6).

We collected five samples from the northern wall of units A and B. The OSL age of  $5.9 \pm 0.4$  ka was obtained from 2009UGR-  
09-O, which is cut by the rupture. For the remaining four samples that are not cut by the rupture, the oldest OSL age is  $1.3 \pm 0.1$

405 ka, recorded for 2009UGR-05-O (Table 1). Additionally, samples were collected from units F (2009UGR-01-C) and A  
(2009UGR-02-C) for radiocarbon dating (Table 2). The radiocarbon age of the charcoal from 2009UGR-02-C is  $160 \pm 30$  cal  
yr BP, which aligns with the OSL age of  $0.15 \pm 0.01$  ka for the sediment containing the charcoal (2009UGR-07-O), and strongly  
indicating that unit A was deposited at this time. Based on the the comprehensive dating analyses, the MRE for this trench  
occurred between  $5.9 \pm 0.4$ – $1.3 \pm 0.1$  ka, as the faulting event took place during the continuous deposition of unit B.



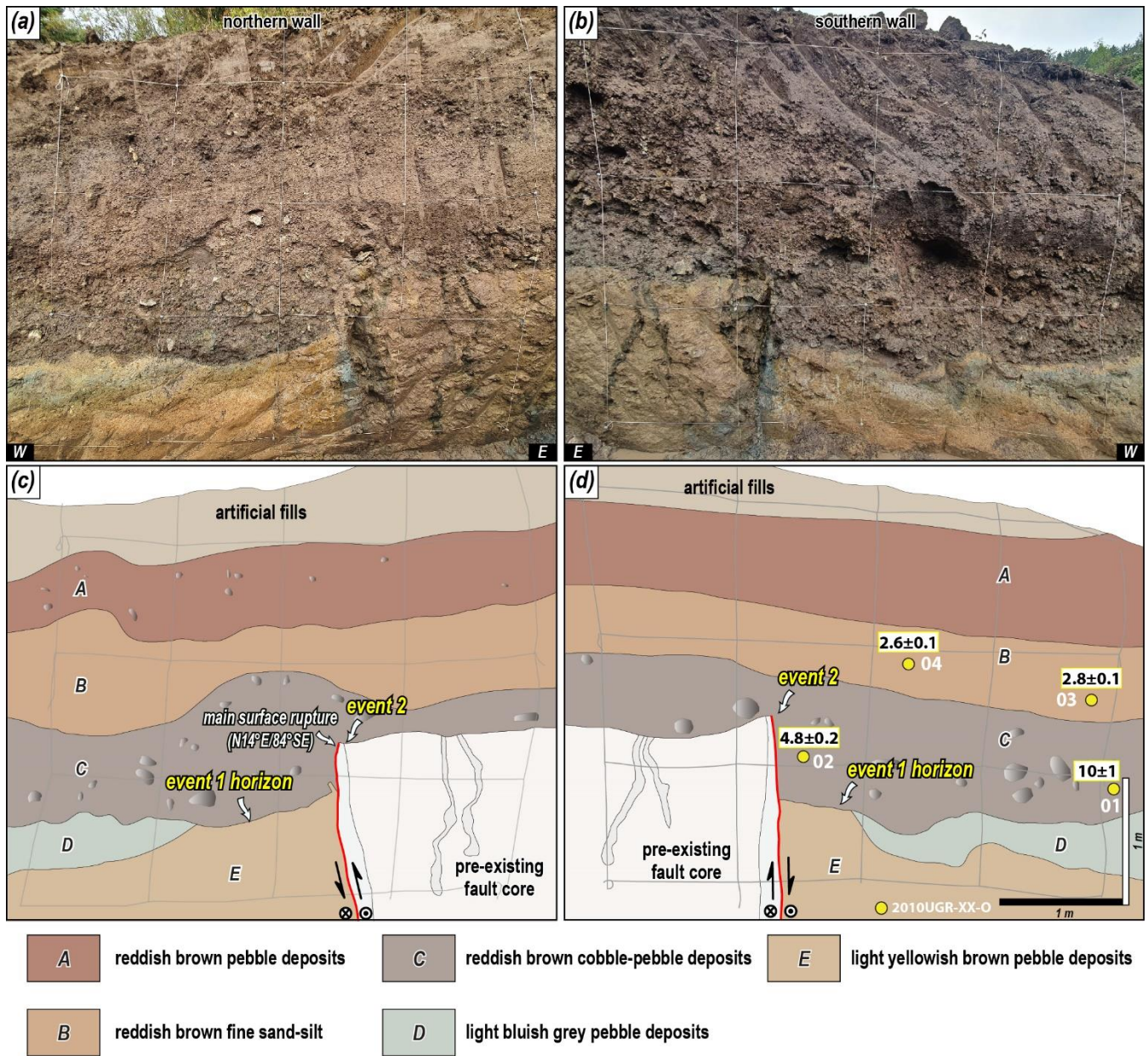
410

Figure 6: Photomosaic of the trench 4 wall of the (a) northern and (c) southern walls. The colored circles represent samples for age dating. Detailed sketch of the trench 4 wall of the (b) northern and (d) southern walls. Grey lines indicate a 1 × 1 m grid. The numbers in the yellow, red, and blue boxes represent OSL and IRSL (ka), radiocarbon (cal yr BP), and ESR (ka) dating results, respectively.

#### 415 4.2.5 Trench 5

Trench 5 is located 40 m north of Trench 4. Because of its proximity, Trench 5 shares identical topographic characteristics with Trench 4, except that it lies on the margins of a hillslope instead of on an alluvial fan. The trench wall contained five Quaternary sedimentary units, cut by one fault splay (Fig. 7). The overall appearance of the exposed wall is similar to that of Trench 4. The hanging wall of the fault splay that cut the Quaternary sediments consists of a pre-existing fault core at least 20 m wide. Where it abuts the Quaternary sediments, a 10 cm wide light grey fault gouge developed, which changed to a yellowish grey fault gouge with yellow clay mixed toward the top. Units A-C show subhorizontal bedding, units D and E show westward-dipping bedding, and there is an angular unconformity between units C and D. Trenches 4 and 5 are almost the same because they are adjacent, with units A-C in Trench 5 matching units A, B in Trench 4 and units D, E in Trench 5 matching units C-F in Trench 4. The reddish-brown sediments in the upper part of Trench 5 appear to be thicker than in Trench 4 because it is the tip of a hillslope. The Quaternary fault splay cut unit C but failed to cut unit B. The slickenline observed on the high-angle Quaternary fault splay indicated a dextral slip with a small reverse component. At least two faulting events are estimated, based on the same angular unconformity as in Trench 4. Event 1 caused units D and E to tilt, which cut them (event 1 horizon, Fig 7). Event 2 occurred during the deposition of unit C, which failed to cut into unit B.

The OSL ages on the southern wall of 2010UGR-03-O and 04-O from unit B are  $2.8\pm 0.1$  and  $2.6\pm 0.1$  ka, respectively, and those of 2010UGR-01-O and 02-O from unit C are  $10\pm 1$  and  $4.8\pm 0.2$  ka, respectively (Table 1). The fault splay is cutting through unit C and failing to cut through unit B. Therefore, trench 5 yielded a tighter MRE range of  $4.8\pm 0.2$ – $2.8\pm 0.1$  ka than the MRE of Trench 4.



435

Figure 7: Photomosaic of (a) northern and (b) southern walls of the Trench 5. The colored circles represent samples for age dating. Detailed sketch of (c) northern and (d) southern walls of the Trench 5. Grey lines indicate a 1 × 1 m grid. The numbers in the yellow, red, and blue boxes represent OSL and IRSL (ka), radiocarbon (cal yr BP), and ESR (ka) dating results, respectively.



### 4.3 Paleo-stress reconstruction

The 20 slickenlines found in the trench are divided into those in the Quaternary slip surface that cut the Quaternary sediments and those in the pre-existing fault core. For the reconstruction of the paleo-stress field, twenty kinematic data along with the geometry of the fault planes and slickenlines were collected and analyzed using Wintensor S/W (v.5.8.5) (Delvaux & Sperner, 2003). Based on the slickenlines of the Quaternary slip surface, the analysis yielded a maximum horizontal stress ( $\sigma_{Hmax}$ ) in the ENE-WSW direction ( $R'=1.62$ ; Delvaux et al., 1997; Fig. 8), which agrees with the current stress field on the Korean Peninsula (Park et al., 2007; Kim et al., 2016; Soh et al., 2018; Kuwahara et al., 2021). The reconstructed paleo-stress indicated that the dextral slip with a small reverse component identified in the Quaternary slip surface occurred under an ENE-WSW oriented  $\sigma_{Hmax}$  with vertical  $\sigma_2$  (strike-slip regime).

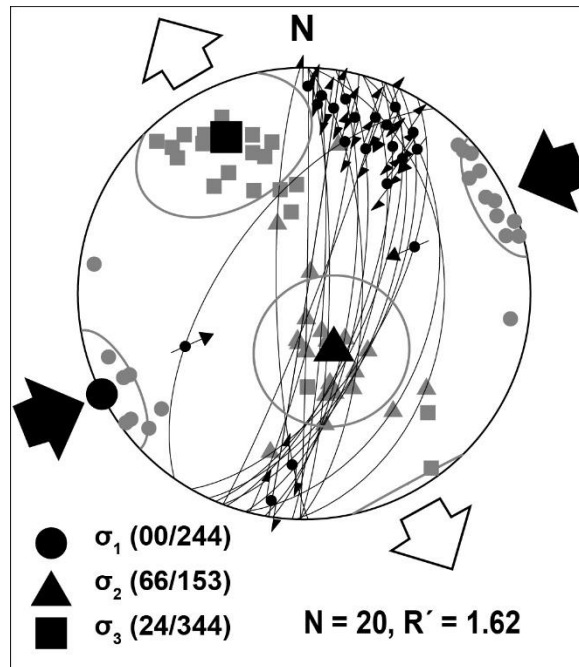


Figure 8: Fault slip data in the Quaternary slip surface (lower-hemisphere, equal-area projection). Convergent and divergent arrowheads represent contraction ( $\sigma_{Hmax}$ ) and horizontal stretching ( $\sigma_{Hmin}$ ) directions, respectively. The principal stress axes  $\sigma_1$  (circles),  $\sigma_2$  (triangles), and  $\sigma_3$  (squares) are projected.  $R'=2-R$  ( $\sigma_2$  is vertical) [Delvaux et al., 1997;  $R=(\sigma_2-\sigma_3)/(\sigma_1-\sigma_3)$ ].

### 4.4 Displacement and Earthquake Magnitude Estimation

The results calculated using the marker, vertical separation of each trench, and Eq. (B1) are listed in Table 5. In the previous study by Lee et al. (2016), the horizontal displacement of the MRE at the Dangu site is determined to be 2.55 m. For each surface rupturing event in Trench 1, the horizontal displacement per event according to the event horizon is 0.9–1.05 m, and the horizontal displacement of the MRE is 1.72 m. Using the bedrock and Quaternary sediments unconformity identified by corings in Trench 2 as a marker, the cumulative horizontal displacement is 76 m. The MRE cutting the colluvial wedge in Trench 3 has a horizontal displacement of 2.85 m. However, when considering the overall interpretation, only the MRE and

AE, but not the PE, are recognized in Trench 3 (Figs. 5 and 9). The displacement cutting the colluvial wedge likely reflects the displacement of the missing PE as well as the MRE, which is supported by the long interval between the wedge (unit D) and the deposit covering the wedge (unit B). Thus, it is reasonable to exclude the calculated displacement as it is unlikely to be the displacement of the MRE. The horizontal displacement of the MRE in Trench 4 and 5 are 0.82 m and 2.21 m, respectively, using the lower boundary of units B and C as markers. Combining the results from each trench, the horizontal displacement of MRE in the study area is 0.82–2.55 m and the cumulative horizontal displacement is 76 m. The horizontal displacement per event is similar, between 0.9–1.05 m for PE and AE (event 1, 2), but the trench shows a higher displacement for the MRE (event 3).

We estimated the maximum earthquake magnitude by applying the MD (horizontal displacement: 0.82–2.55 m) of the MRE, resulting in a maximum magnitude estimate 6.7–7.1. Seismic SSDs such as the 20–50 clastic dike and 30 cm ball-and-pillow structure observed in the exposed wall (units E and G in Trench 1; unit F in Trench 3), serve as indirect evidence indicating an earthquake of at least magnitude 5.5 (Atkinson et al., 1984).

**Table 5. Fault displacement of study area**

|                       |                         | $S_v$ (m)                     | $\alpha$ (°) | $\gamma$ (°) | $S_t$ (m) | $S_h$ (m)   |
|-----------------------|-------------------------|-------------------------------|--------------|--------------|-----------|-------------|
| Dangu <sup>a</sup>    | MRE (event 3)           | 0.67                          | 79           | 15           | 2.64      | <b>2.55</b> |
|                       | Marker                  | Unit D                        |              |              |           |             |
| Trench 1 <sup>b</sup> | MRE (event 3)           | 0.49                          | 69           | 17           | 1.8       | <b>1.72</b> |
|                       | Marker                  | Unit C                        |              |              |           |             |
|                       | PE (event 2)            | 0.31                          | 75           | 17           | 1.1       | <b>1.05</b> |
|                       | Marker                  | Unit G                        |              |              |           |             |
|                       | AE (event 1)            | 0.22                          | 53           | 17           | 0.94      | <b>0.9</b>  |
|                       | Marker                  | Unit H                        |              |              |           |             |
| Trench 2              | Cumulative displacement | 34                            | 38           | 36           | 94        | <b>76</b>   |
|                       | Marker                  | Quaternary deposits thickness |              |              |           |             |
| Trench 3              | MRE (event 3)           | 1.1                           | 42           | 30           | 3.29      | <b>2.85</b> |
|                       | Marker                  | Unit D                        |              |              |           |             |
| Trench 4              | MRE (event 3)           | 0.25                          | 86           | 17           | 0.86      | <b>0.82</b> |
|                       | Marker                  | Unit B                        |              |              |           |             |
| Trench 5              | MRE (event 3)           | 0.8                           | 84           | 20           | 2.35      | <b>2.21</b> |
|                       | Marker                  | Unit C                        |              |              |           |             |

<sup>a</sup>modified from Lee et al., 2015

<sup>b</sup>modified from Song et al., 2020

## 5 Discussion

### 475 5.1 Interpretation of Paleoseismic Data

#### 5.1.1 MRE and number of surface faulting

We determined the MRE and number of faulting events of the study area, considering previous studies, the age of Quaternary deposits and fault gouges, the geometry and cross-cutting relationship between fault splays and sediments, and the kinematics in each trench (see the heading 4.1). The results for each trench are synthesized to estimate the MRE, number of earthquakes (faulting events), and timing of earthquakes along the Byeokgye section (Fig. 9). First, the MRE is  $3.2 \pm 0.2$ – $2.8 \pm 0.1$  ka, which is the time of overlap in several trenches. Considering the error range, the surface rupture must have occurred approximately 3,000 years ago. Considering the minimum number of earthquakes estimated for each trench as the maximum, at least three faulting events may have occurred along the studied section. Furthermore, the penultimate earthquake (PE) occurred in  $75 \pm 3$ – $17 \pm 1$  ka, based on the youngest age of the PE (unit C) from Trench 1 and the MRE from the Byeokgye site (Fig. 9). The antepenultimate earthquake (AE) is from  $142 \pm 4$ – $137 \pm 3$  ka, constrained by the paleoseismic interpretation in Trench 3. On the other hand, clustering the ESR ages at each trench with an error range suggests at least three separate older earthquakes at  $817 \pm 10$ ,  $404 \pm 10$ , and  $245 \pm 37$  ka (Fig. 9). These ages indicate the time elapsed since the ESR signal is set to zero by the faulting at depth, but it needs much care to use as a timing indicator of the faulting event because of the possibility that the ESR signal is not completely bleached. Nevertheless, clustered faulting patterns at seven sites suggest that the study area had at least six earthquakes during the Quaternary.

480  
485  
490

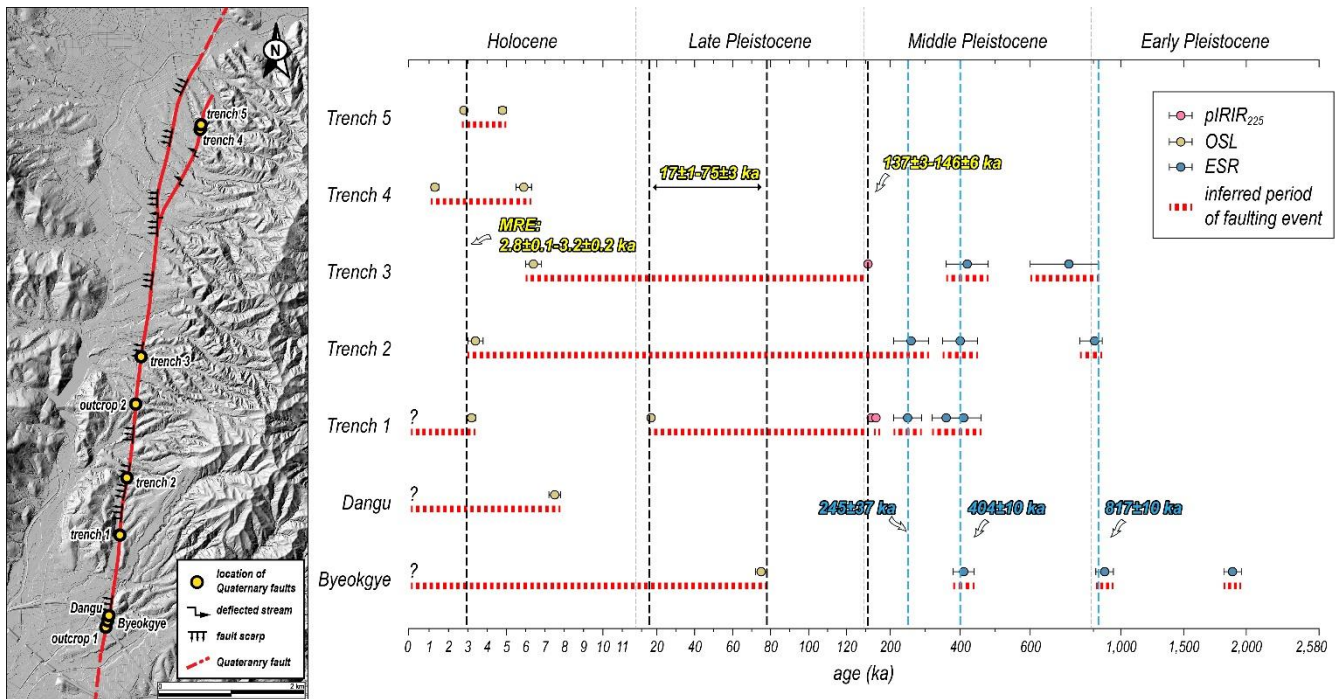


Figure 9: Age distribution graph of the study area. The graph reveals the timing of the paleo earthquake based on trench interpretation and age overlap. The most recent earthquake in the study area occurred probably around 3,000 years ago.

### 495 5.1.2 Quaternary slip rate and recurrence interval

The slip rate is an expression of the average displacement of a fault over a certain period, which numerically shows how quickly energy (stress) accumulates in a fault zone and is used as an important input parameter in seismic hazard assessment (Liu et al., 2021). The horizontal slip rate in the study area is calculated based on the earthquake timing and horizontal displacement of each trench. We calculated slip rates from three trenches spanning different periods: Late Pleistocene to  
 500 Holocene (Trench 1), Quaternary (Trench 2), and Middle Pleistocene to Holocene (Trench 3). In Trench 1, we derived a slip rate of 0.12–0.14 mm/yr based on the horizontal displacement of MRE of 1.72 m and the  $13.8 \pm 1.2$  ka time interval between MRE and PE (time gap between units B and C; Table 1). For Trench 2, borehole data revealed a slip rate of 0.02–0.03 mm/yr, calculated from the cumulative horizontal displacement of 76 m and the cosmogenic  $^{10}\text{Be}$ - $^{26}\text{Al}$  isochron burial age of  $2.87 \pm 0.59$  Ma from the lowermost Quaternary deposits. In Trench 3, we calculated a slip rate of 0.02 mm/yr using the 2.85 m horizontal  
 505 displacement of the event that cut the colluvial wedge (unit D) and the  $130.6 \pm 3.4$  ka time interval between events (time gap between units B and D).

Considering the age of the deposits, the slip rate of 0.12–0.14 mm/yr from Trench 1 represents movement during the Holocene, while the rates from Trenches 2 and 3 may represent cumulative slip rate (0.02 mm/yr) throughout the Quaternary. As noted in the method section (3.3), there are uncertainties in obtaining slip rates from 2D trenches alone on strike-slip faults such as

510 the study area. In particular, the discontinuous distribution of Quaternary sediments may have led to a misestimation of the slip rate. There are two distinct types of sediments in the trench wall: (1) light brown, sediments of mid-to-late Pleistocene age, which tend to be tilted in the vicinity of the surface rupture, and (2) dark brown, nearly horizontal Holocene sediments (Table 1, Figs. 3-7). The exact time interval between these two deposits is unknown; however, there is unconformity, and the MRE mostly cut Holocene sediments (<10,000 years). A depositional gap, such as an unconformity, causes earthquake records to  
515 be missed during that time, leading to a misestimation of the slip rate. For this reason, in strike-slip fault settings, 3D trenching should be used because the slip rate using displacement from 2D trenches is underestimated compared to the slip rate using topography, which preserves most of the displacement. The slip rates in this study (0.12–0.14 mm/yr) are lower compared to the slip rates derived from the topography and 3D-trench reported in the study area of 0.38–0.57, 0.5 mm/yr, respectively (Kim et al., 2024; Naik et al., 2024). Nevertheless, the slip rates in our study are meaningful as a minimum value that establishes a  
520 lower boundary for the slip rates in the study area.

The recurrence interval in the study area is also estimated. Based on the minimum of three earthquakes estimated from the number of faulting events, the interval between the MRE and PE is 14–72 ka and between the PE and AE is 62–129 ka (Fig. 9). The recurrence interval (RI) can be calculated using the slip rate and event per displacement ( $RI = \text{event per displacement} / \text{slip rate}$ ; Wallace, 1970). For MRE, using the slip rate (average 0.13 mm/yr) and event per displacement (1.72 m in Trench 1), the  
525 RI is approximately 13 ka. Using the displacement per event (average 0.98 m) and long-term slip rate (0.02 mm/yr) for PE and AE, the RI is roughly 49 ka. The RI between MRE and PE is similar to the minimum value of the time gap shown in Figure 9 and the value estimated by the slip rate. Between PE and AE, the recurrence interval calculated from the slip rate is smaller than the time gap obtained in Figure 9. It suggests that the earthquake records in the trench are not complete. Therefore, we can make a conservative estimate that the recurrence interval of the study area is over 13,000 years. Although no clear  
530 recurrence interval has been presented in Korean paleoseismic studies, Kim and Lee (2023) used ESR ages to suggest that the Yangsan Fault follows a quasiperiodic model and has a recurrence interval of approximately 100 ka, which is closely related to the interval of interglacial sea-level loading over the Late Quaternary. However, the recurrence interval may be shorter if the complexity of the fault distribution is combined with external factors, such as increased seismicity on the Korean Peninsula after the Tohoku Earthquake (Hong et al., 2015; 2018) or changes in slip rates.

## 535 **5.2 Structural patterns of Quaternary reactivation of the Yangsan Fault**

The trenches revealed the following common features. First, the hanging wall of the Quaternary slip surface is mostly deposited with Holocene sediments only, with no Middle Pleistocene sediments present. This indicates that reverse faulting has occurred continuously since at least the Middle Pleistocene. Second, NNE to N-S striking Quaternary slip surfaces with high-angle dip have rakes of 20° or less, indicating dextral slip with a minor reverse component. Third, the main surface rupture has a top-to-  
540 the-west geometry, and its hanging wall consists of a pre-existing fault core in all trenches. Fieldwork and previous studies revealed that the A-type alkaline granite in the study area is a dextral offset marker of the Yangsan Fault (Hwang et al., 2004,

2007a, b), and vertically drilled borehole from the footwall of Trench 2 revealed that the basement rock is A-type alkali granite. In addition, Kim et al. (2022) conducted inclined borehole drilling and microstructural studies in the vicinity of Trench 1 and identified a fault damage zone, undeformed wall rock, and a fault core approximately 25 m wide on the eastern side of the A-type alkali granite. Multiple lines of evidence demonstrate that the pre-existing fault core distributed on the trenches is the main fault core zone of the Yangsan Fault cutting the A-type alkali granite and that the western boundary of the main fault core is reactivated during the Quaternary. The slip surface where the A-type alkali granite contacts the main fault core suggests that it is in a more slip-prone state (e.g., low coefficient of friction, foliated smectite-rich slip zone; Woo et al., 2015; Kim et al., 2022) during the Quaternary than other slip surfaces within the fault core. Taken together, these results demonstrate that the western boundary of the fault core within the Yangsan Fault zone has been reactivated as a dextral slip with a small reverse component since at least the Early Pleistocene, causing surface rupture in the study area.

A Quaternary surface rupture with a top to the west geometry and its hanging wall composed of fault core is characterized not only in the study area but also throughout the Yangsan Fault. All Quaternary fault sites on the Yangsan Fault, except for the Bogyongsan site (top-to-the-east, BGS in Fig. 10; Lee et al., 2022), show the top-to-the-west geometry of the main surface rupture (Kyung, 2003; Choi et al., 2012; Cheon et al., 2020a; Han et al., 2021; Ko et al., 2022; Lim et al., 2022; Kim et al., 2023). At the Quaternary fault sites north of the study area, pre-existing fault cores are observed on the hanging wall of the main slip surface (Kyung, 2003; Choi et al., 2012; Han et al., 2021; Lee et al., 2022; Ko et al., 2022; Lee, 2023). The deformation pattern of the Quaternary faulting of the Yangsan Fault is top to the west, with the main fault core and unconsolidated sedimentary layers abutting the main surface rupture.

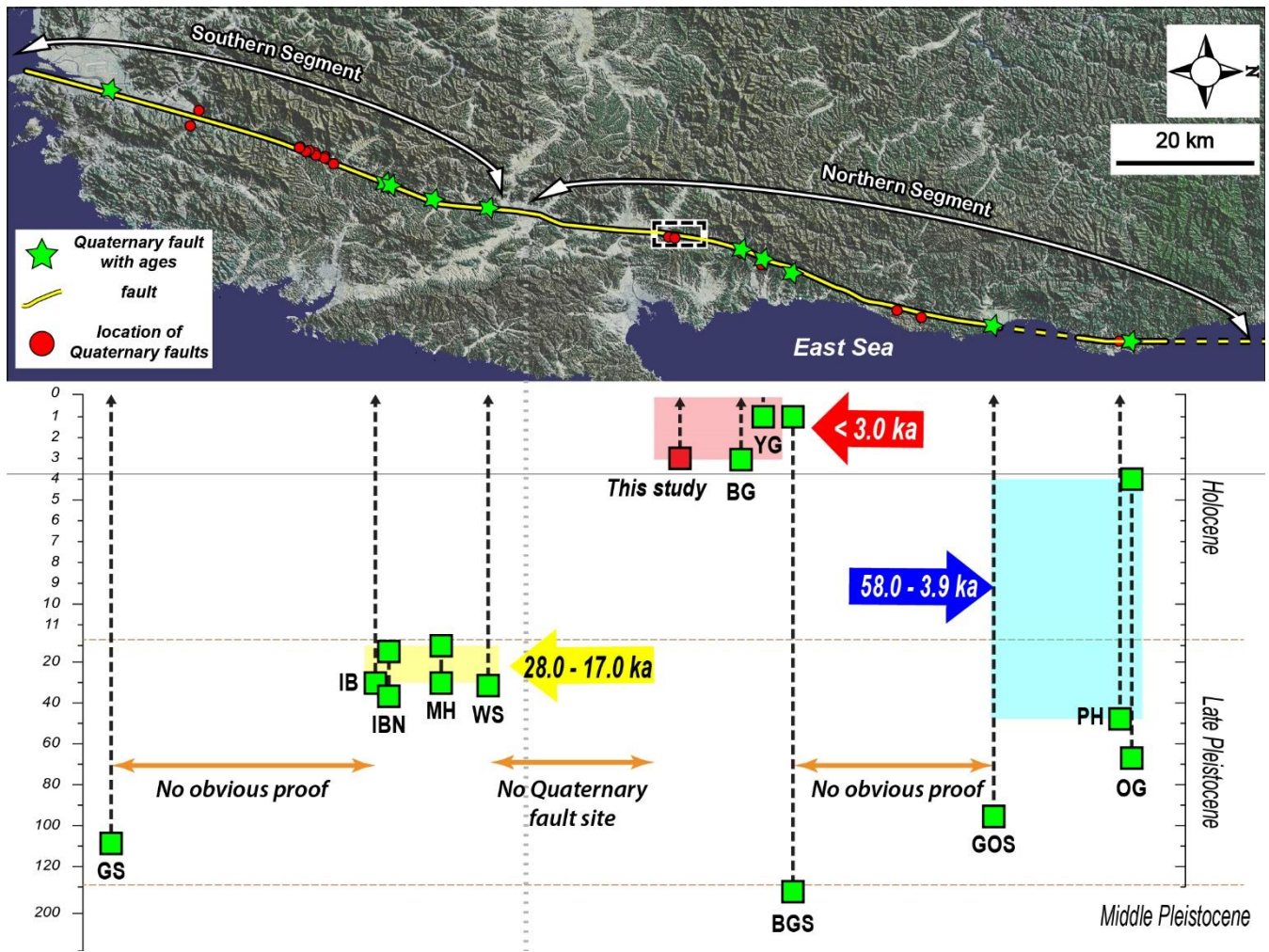


Figure 10: MRE of Yangsan Fault. Green stars indicate where MREs have been identified due to the presence of Quaternary sediment ages. GS: Gasan (Lim et al., 2022), IB: Inbo (Cheon et al., 2020a), IBN: Inbonorth, MH: Miho, WS: Wolsan (Kim et al., 2023), BG: Bangok (Lee, 2023), YG: Yugye (Kyung, 2003), BGS: Bogyongsa (Lee et al., 2022), GOS: Goesi (Ko et al., 2022), PH: Pyonghae (Choi et al., 2012), OG: Ogok (Han et al., 2021). "No obvious proof" refers to areas where sites that cut unconsolidated sediments are present but not dated.

### 5.3 MRE and activity for each segment of the Yangsan Fault

The MRE of the Yangsan Fault is analyzed section-by-section by synthesizing previous studies (Fig. 10). The Bangkok (BG) and Yugye (YG) sites adjacent to the north of the study area have similar MREs. The Bangkok site, which is closest to the study area, shares the same MRE, after 3,000 years ago (Lee, 2023), while the Yugye site has the youngest MRE along the entire Yangsan Fault, after AD 646 (Kyung, 2003). It is clear that the section from the study area to the Yugye site, including the Bangkok site, is the most recently ruptured section of the Yangsan Fault, with the last surface rupture occurring approximately <math>< 3.0\text{ ka}</math> (red arrow in Fig. 10). The Bogyongsa (BGS) site, north of the Yugye site, has an MRE of Middle Pleistocene and Holocene (Lee et al., 2022). The Yeongdeok area, which extends from the northern part of the Bogyongsa site to Goesi (GOS)

575 site, has several reported Quaternary fault sites though no conclusive evidence of Quaternary faulting exists. This is due to  
either the cutting of unconsolidated sediments without age constraint or the lack of displacement of unconsolidated sediments,  
with only ESR ages available for the fault gouge (Choi et al., 2012). The MREs at the Ogok (OG), Pyeonghae (PH), and Gosi  
sites in the northernmost region of the northern Yangsan Fault date to both Late Pleistocene and Holocene (Choi et al., 2012;  
Han et al., 2021; Ko et al., 2022). Overall, the northern part of the Bogyongsan site (the northern part of the Northern Yangsan  
Fault) experienced MREs between the Late Pleistocene and the Holocene. The Angang area beyond the south of the study area  
580 has no reports of Quaternary faulting and at the Wolsan (WS) site, in the northernmost part of the southern Yangsan Fault, the  
MRE is Late Pleistocene. The Miho (MH), Inbonorth (IBN), and Inbo (IB) sites of the southern Yangsan Fault are all Late  
Pleistocene and the southernmost part of the Yangsan Fault, the Gasan (GS) site, is after the Late Pleistocene (Lim et al., 2021).  
The Southern Yangsan Fault from the Wolsan site to the Gasan site experienced MREs mostly in the Late Pliocene. At first  
glance, it may appear that the section between Yugye and the study area is more active with Holocene MREs but the timing  
585 of the MREs alone is inadequate to assess which zone is more active. For example, Holocene surface rupture may indicate that  
the fault has a short recurrence interval; conversely, a fault with an older MRE may have a higher potential for future  
earthquakes because recent faulting events may have released stress accumulation. Deviation in the timing of MREs at different  
sites or sections can be a direct indication of the fault motion that caused the surface rupture; however, uncertainty in age  
constraints due to the presence or absence of sediments must be considered. The MRE is an important factor in activity  
590 assessment because if it has a recurrence interval, the elapsed time can be calculated, which can be used to predict future  
earthquakes. However, the activity considered using MRE alone can be misleading; therefore, it is necessary to derive  
recurrence intervals and elapsed time to accurately predict earthquakes based on paleoseismic data. Ultimately, activity  
assessment should consider not only paleoseismic data but also topographic, structural, seismic, and geodetic aspects.

## 6 Conclusion

595 We conducted surface geological surveys, trenching, coring, OSL/IRSL dating, radiocarbon dating, ESR dating, and  
cosmogenic nuclides dating along the lineament extracted from topographic analysis using high-resolution LiDAR imagery at  
the Yangsan Fault. The primary aim is to identify the surface ruptures that occurred during the Quaternary period, derive  
structural features, and gather paleoseismic data for the Quaternary surface rupture. The main conclusions are as follows:

(1) A comprehensive analysis, combining two previously reported Quaternary fault sites (Byeokgye and Dangu), two newly  
600 discovered natural outcrop sites, five trenches, coring surveys, and dating of unconsolidated sediments, charcoal, and fault  
rocks, revealed a 7.6 km Quaternary surface rupture along the Yangsan Fault. (2) The Quaternary surface ruptures in the study  
area exhibited an east-dipping geometry with an N-S to NNE strike and moved as a dextral slip with a reverse slip component  
during the Quaternary. (3) At least six faulting events are interpreted from the trench walls, with an MRE of approximately  
3,000 years ago. The MRE horizontal displacement ranged from 0.82 to 2.55 m, cumulative horizontal displacement from 76  
605 m, horizontal displacement per event before the MRE from 0.9 to 1.05 m, and maximum magnitude using the MD from  $M_w$



6.7–7.1. The slip rate is 0.12–0.14 mm/yr, with a recurrence interval of at least 13,000 years. (4) The Quaternary structural features indicate that during the Quaternary period, the western boundary of the main fault core of the Yangsan Fault is reactivated under ENE-WSW compressional stress. The top-to-west geometry is consistent with that observed throughout the Yangsan Fault. (5) The southern part of the northern Yangsan Fault, including the study area, documents a Holocene MRE that is younger than those documented in the southern Yangsan Fault.

610 Surface rupturing has been observed along most sections of the Yangsan Fault and in the study area, and basic paleoseismic studies continue to be reported (Fig. 10; Lee et al., 2022; Kim et al., 2023). The challenge is that Korea's geologic diversity results in a large number of faults that need to be studied (e.g., Chugaryeong Fault). Only then will it be possible to properly understand the seismicity pattern of Korea and the earthquakes in the low active intraplate regions. Although the study results are only for a small 10 km section of the Yangsan Fault with a 200 km extension, the San Andreas Fault, which has high-resolution paleoseismic data from more than 200 trenches, also started out in the same way. In particular, studying seismic hazards on the Korean Peninsula, with its urbanization, cultivated land, slow slip rates, long recurrence intervals, and fast erosion rates, is a challenge. This research will hopefully contribute to the research on earthquake hazards in Korea, which is just beginning to advance. Furthermore, this study contributes valuable insights for seismic hazard assessment in the region and offers a broader understanding of intraplate earthquake dynamics, thereby aiding earthquake prediction efforts.

615  
620

## Appendices

### Appendix A. Geomorphic map of the study area

The topography of the study area in Ha et al. (2022) is summarized as follows:

625 The study area's topography is divided into a lowland area to the west and a mountainous region to the east (Fig. A1). The eastern mountains, the ridges extending from the summit are cut off by a lineament heading west, which influences the drainage system, with streams flowing from the high elevations east to the west. Alluvial fans, formed from sediments from the eastern mountains, are found at the base of the slopes. Twelve lineaments are identified, with the main lineament, which extends for 7.6 km, displaying high activity through the northern part of the Byeokgye site. Subsidiary high-activity lineaments and low-activity lineaments, mainly following N–S or NNE directions, are present, though many are valleys formed by erosion rather than rupturing. The main lineament exhibits continuous fault scarps and deflected streams, with reservoirs often located along it due to impermeable fault gouges that enable water storage. Topographic analysis revealed fault scarps, knickpoints, and displacement features along the main lineament, particularly visible in LiDAR data. Fault scarps are continuously and distinctly visible in the main lineament of the southern region (Fig. A2). In the cross-section, the fault scarps are recognized as knickpoints, and on the topographical map, the ridges on the east side of the lineament are cut by the surface rupture and merged with the alluvial fans. The main lineament of the northern region is identified as a linear arrangement of deflected streams and fault scarps (Fig. A3). Unlike in the south, the fault scarps in the north show surface uplift estimated at a vertical offset of between 2–4.2 m of the same alluvial fan surface cross-section. Differences between the southern and northern regions are observed, with the north showing vertical offsets of 2–4.2 m and more pronounced faulting. The horizontal offsets calculated based on the three deflected streams are 92 m, 98 m, and 150 m. The tendency for the offset to decrease as the distance from the main lineament increases indicates that the fault offset branching from the main surface rupture gradually decreases.

630

635

640

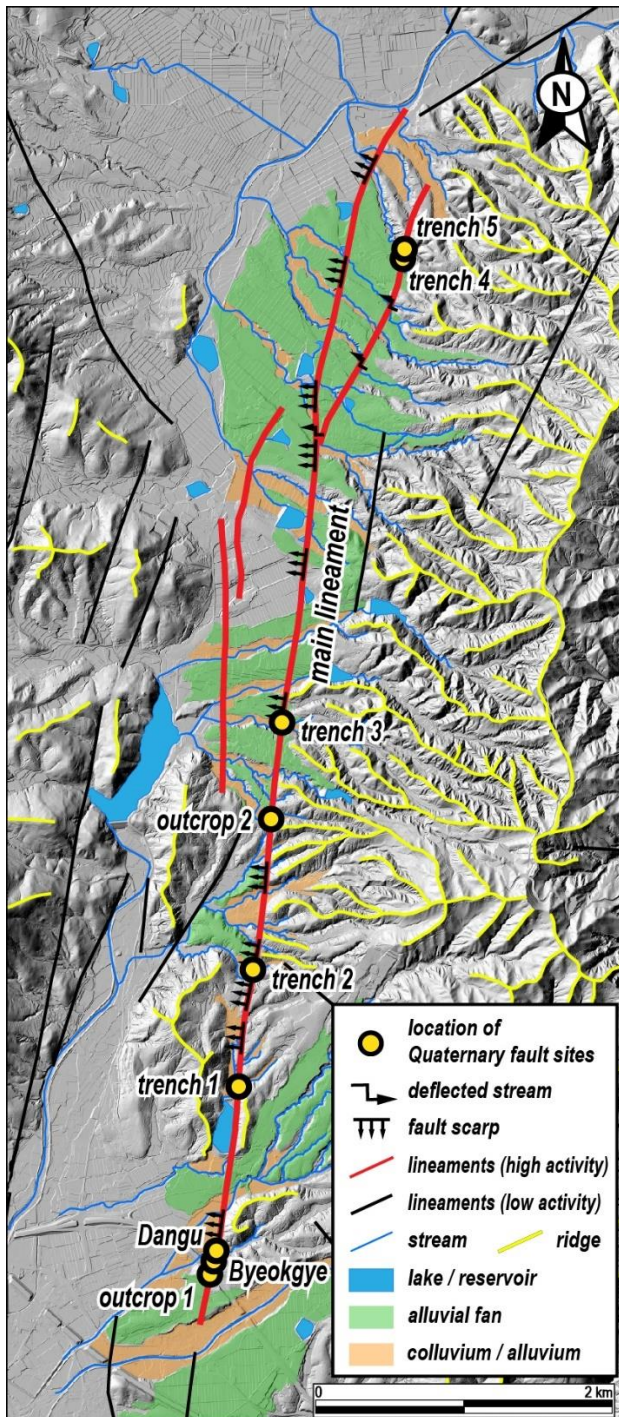


Figure A1: The geomorphologic map of the study area (modified from Ha et al., 2022).

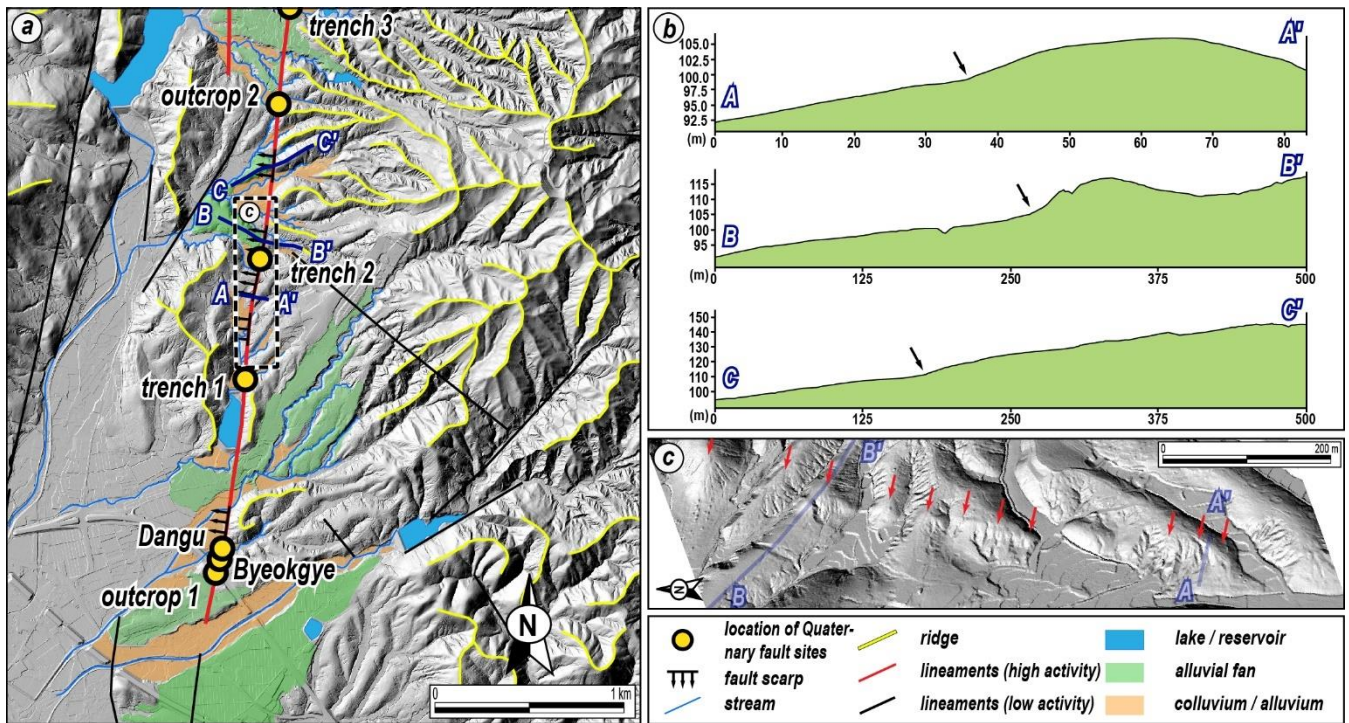
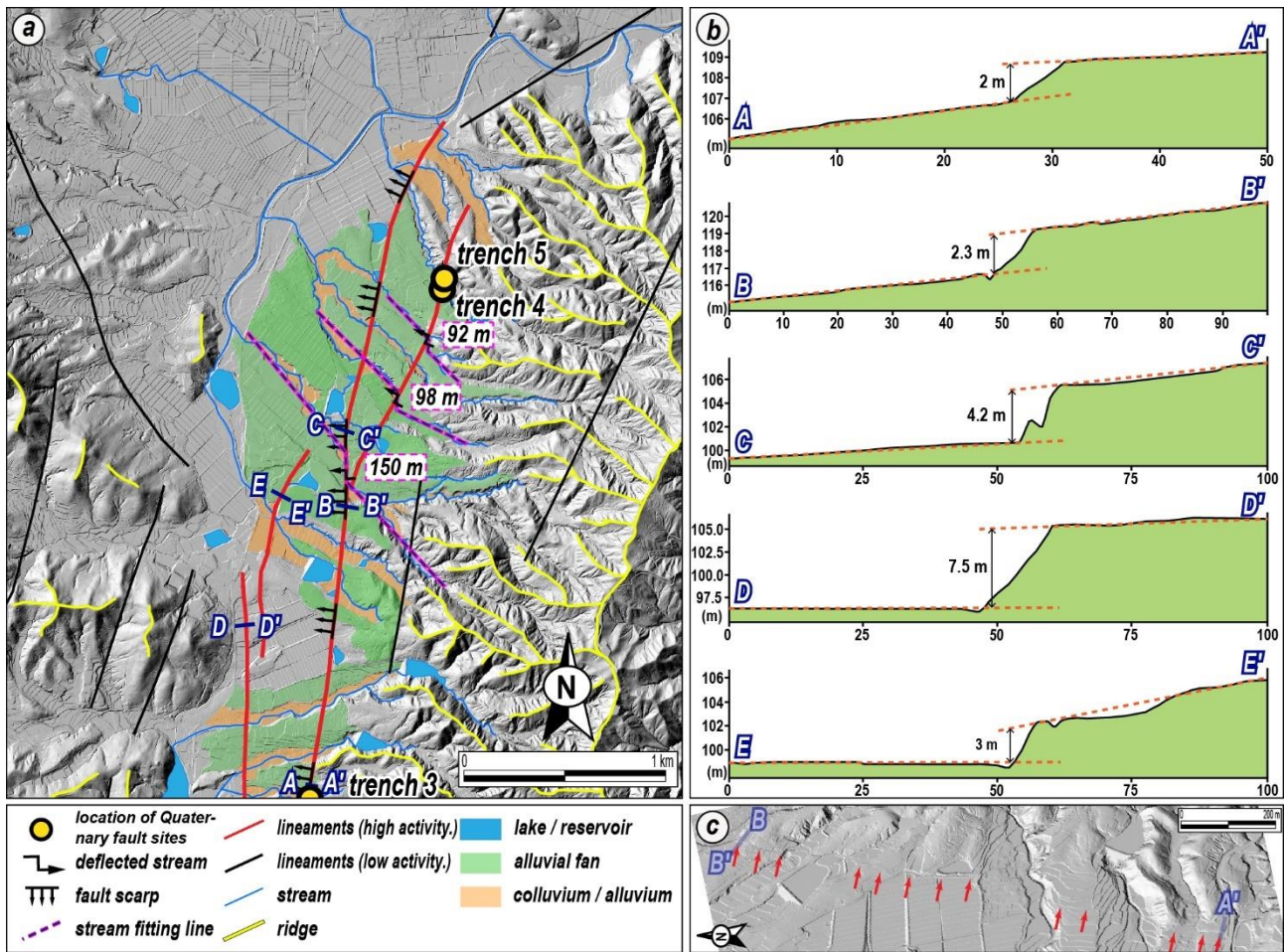


Figure A2: (a) A detailed topographic map of the southern region. (b) Topographic profiles along the main lineament (blue line in (a)) crossing the fault scarps. Black arrows mark knickpoints identified as fault scarps. (c) A 3D hillshade image. The red arrows highlight the fault scarp, which is clearly visible to the unaided eye (modified from Ha et al., 2022).



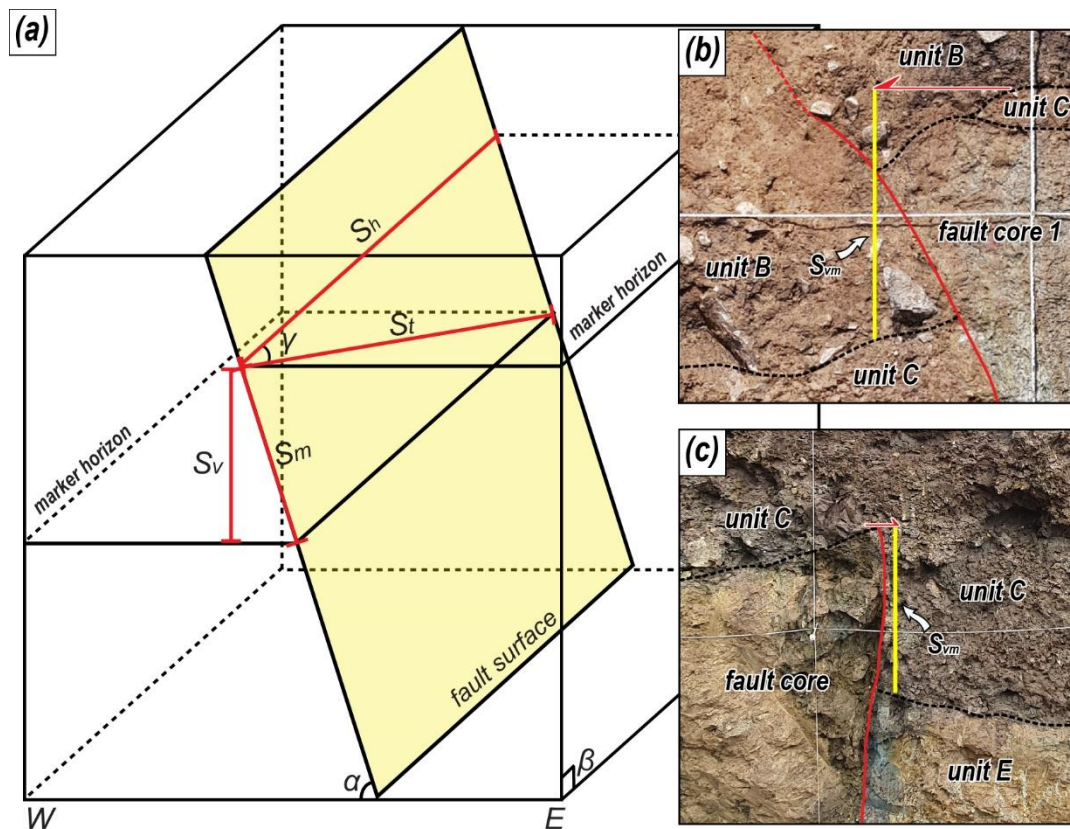
650 Figure A3: (a) A detailed topographic map of the northern region. An NNE lineament branching off from the main lineament is shown by the dextrally deflected stream. (b) Topographic profiles along the line (blue line in (a)) crossing the fault scarps. Fault scarps in the northern region are evident due to the elevation difference in the alluvial fan surfaces. (c) A 3D hillshade image. Red arrows highlight the fault scarp (modified from Ha et al., 2022).

The horizontal displacement ( $S_h$ ) can be calculated using a trigonometric function that considers the vertical displacement ( $S_v$ ), fault dip angle ( $\alpha$ ), rake ( $\gamma$ ), true displacement ( $S_t$ ) and their relationships (Fig. B1; Eq. B1). Assume that the attitude of the marker in the exposed wall at each trench is nearly horizontal in three dimensions and the angle ( $\beta$ ) of the exposed wall is nearly vertical, then the two factors are perfectly horizontal and vertical, respectively. Thus, the vertical separation ( $S_{vm}$ ) and vertical displacement ( $S_v$ ) measured in the exposed wall are equal.

Therefore,

$$S_{vm} = S_v, S_m = \frac{S_v}{\sin \alpha}, S_t = \frac{S_m}{\sin \gamma}, S_h = \cos \gamma * S_t \quad (\text{B1})$$

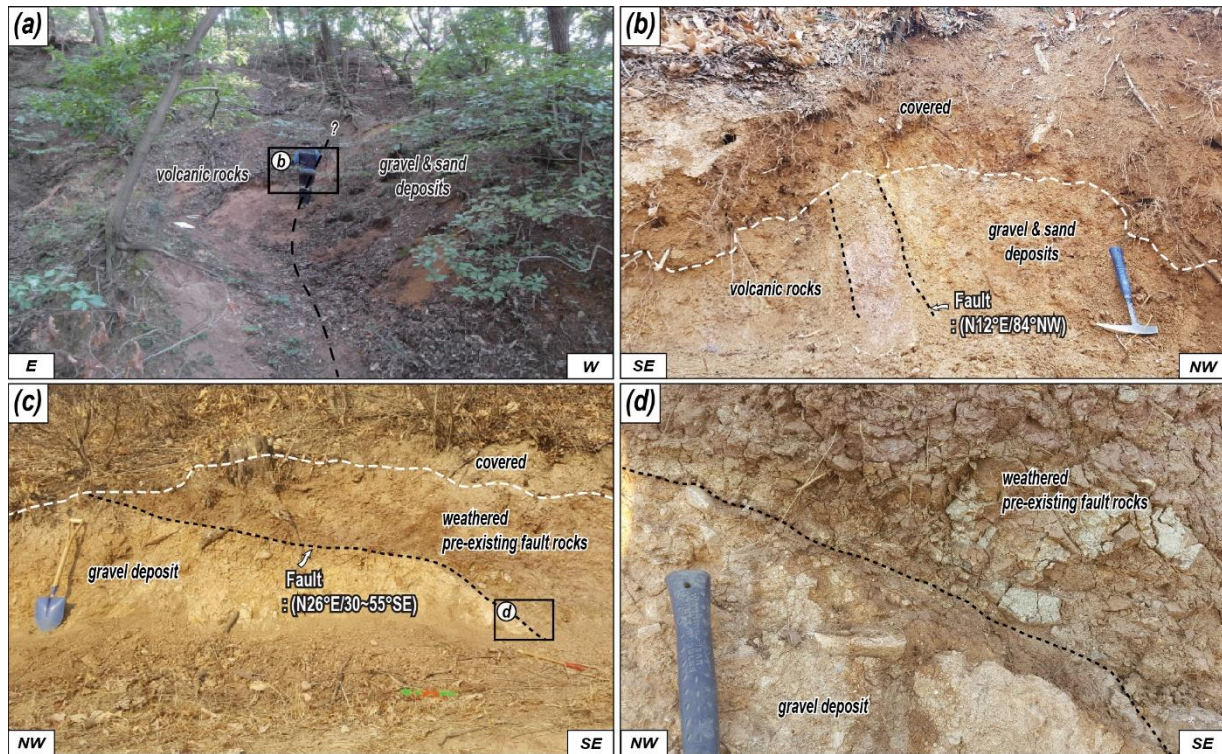
We calculate horizontal displacement ( $S_h$ ) using Eq. (B1) for vertical separation ( $S_{vm}$ ) of the marker measured in the exposed wall, as shown in Table 5.



665

Figure B1: (a) Schematic diagram showing how to calculate true displacement.  $S_h$ : horizontal displacement,  $S_t$ : true displacement,  $S_v$ : vertical displacement,  $S_m$ : dip separation,  $\alpha$ : dip of fault surface,  $\beta$ : dip of cut slope,  $\gamma$ : rake of the striation (modified from Xu et al., 2009). (b and c) Photographs showing the measured vertical separation of the trenches 1 and 5.  $S_{vm}$ : vertical separation.

Outcrop 1 is located 30 m south of the Byeokgye site (Fig. 2c). A high-angle rupture cut the Cretaceous volcanic rocks and unconsolidated sediments interbedded with gravel deposits and sand layers (Fig. C1a). The rupture trace is partially recognized on the surface based on the lithological distribution. The fault core consisted of a 20 cm-wide breccia with a Quaternary slip surface attitude of N12°E/84°NW, and no clear slickening is observed (Fig. C1b). Outcrop 2, on the extension of the main  
 675 lineament, is located 2.7 km north of the Byeokgye site (Fig. 2c). The outcrop contained highly weathered purple sedimentary rock overlying unconsolidated sediments (Fig. C1c). The NNE-striking fault splay dipped toward the east with a low angle. The purple sedimentary rock of the hanging wall is mostly clayey and may be either a pre-existing purple fault gouge or weathered purple Cretaceous sedimentary rock. The fault core adjacent to the unconsolidated deposits consisted of a 2–3 cm thick foliated fault gouge (Fig. C1d). The foliation is subparallel to the slip surface. The unconsolidated gravel deposits have  
 680 poor sorting, and angular clasts consist of sandstone, granitic, and volcanic rocks. No clear slickenlines are observed, owing to highly weathered outcrop conditions. We could not date either outcrop because the clast-rich sediments are not suitable for OSL dating and did not include organic material for  $^{14}\text{C}$  dating.



685 **Figure C1: Photographs showing the outcrops of the rupture which that cut the unconsolidated sediments. (a) Rupture trace on the surface. (b) NNE striking rupture cut the boundary between volcanic rocks and gravel and sand deposits. The fault rock is composed of breccia. (c) Weathered pre-existing fault rocks thrust gravel deposits along the low-angle surface rupturing. (d) Close-up photograph of the rupture. A 2-3 cm thick fault gouge forms a boundary between two different rocks.**

Appendix D. Coring at the Trench 2

690 We cored the footwall of Trench 2. Unconsolidated sand and gravel deposits alternated up to 24 m below the surface. From 24 m to 32.8 m, the material consisted of a granite wash, at the base of which a 1.2 m thick weathering zone is recognized. From 34 m onwards, the bedrock is clearly identified as A-type alkaline granite (Fig. D1). We performed  $^{10}\text{Be}$ - $^{26}\text{Al}$  isochron burial dating on the granite wash immediately above the basement rock.



695 **Figure D1:** Photograph showing drilled core. The lowermost of the unconsolidated sediments, the granite wash, directly overlies bedrock. Cosmogenic  $^{10}\text{Be}$ - $^{26}\text{Al}$  isochron dating samples are taken from this granite wash.



The graphs of the detailed results of 1–2 representative samples per trench for quartz OSL and pIRIR<sub>255</sub>. We selected samples  
 700 from sediments cut into the MRE and from sediments overlying the MRE. The graphs include decay curves, probability density  
 graphs, and <sup>10</sup>Be-<sup>26</sup>Al isochron graphs. The tables also include dose rates, equivalent doses, and luminescence ages of the  
 samples from each trench.

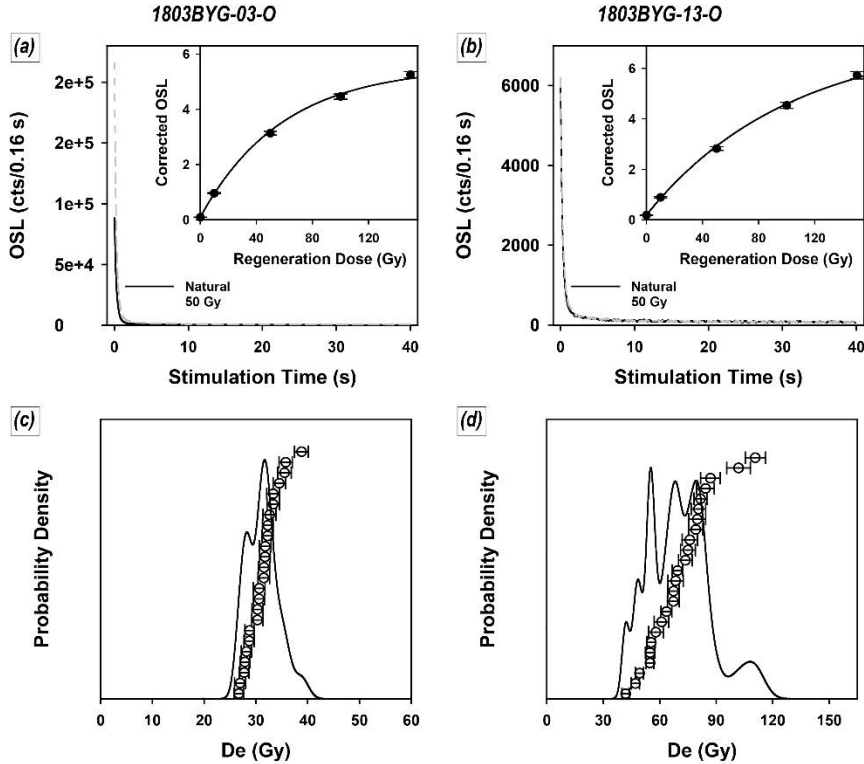


Figure E1: Representative quartz OSL decay curves (a, b) and probability density graph (c, d) of Trench 1.

705

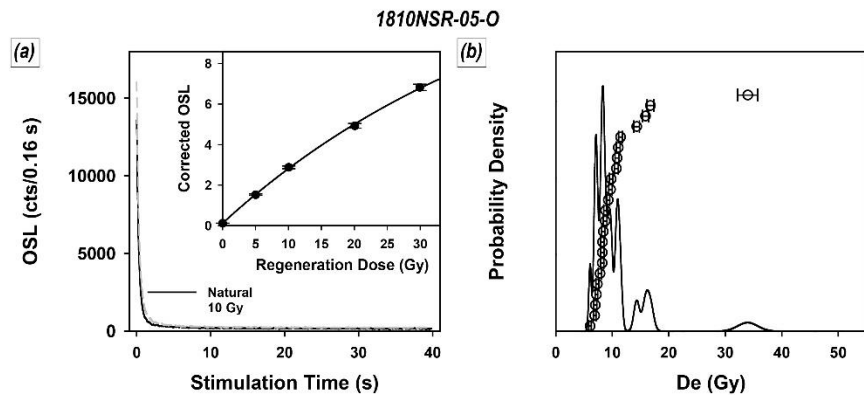


Figure E2: Representative quartz OSL decay curves (a, b) and probability density graph (c, d) of Trench 2.

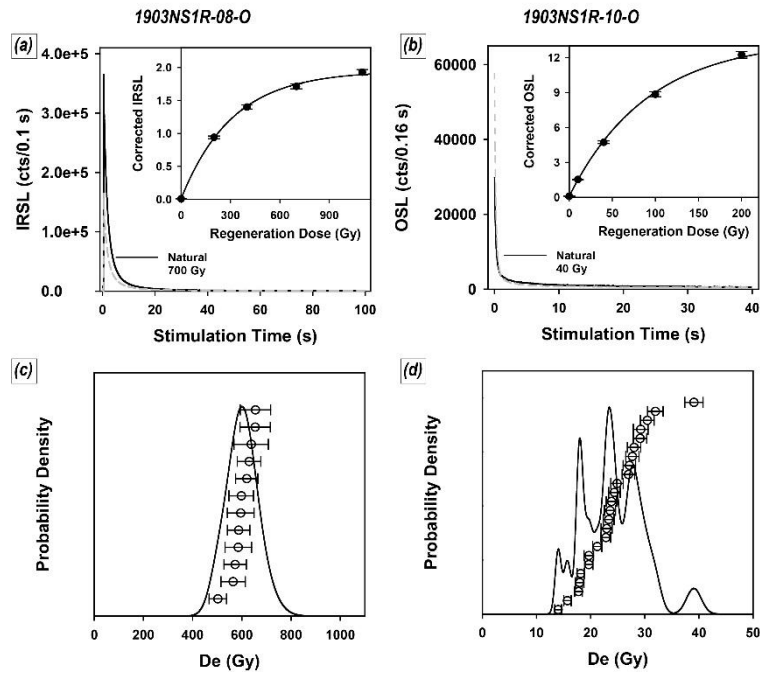


Figure E3: Representative quartz OSL/IRSL decay curves (a, b) and probability density graph (c, d) of Trench 3.

710

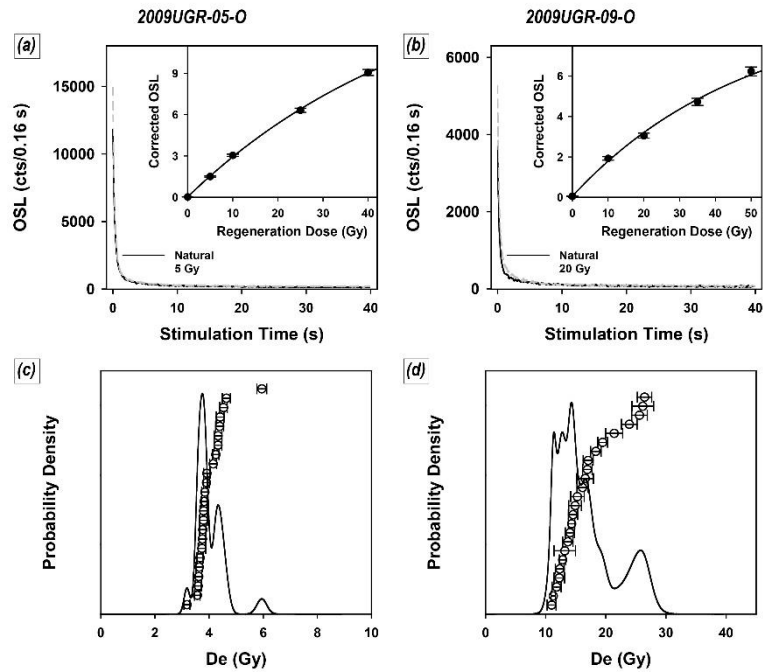


Figure E4: Representative quartz OSL decay curves (a, b) and probability density graph (c, d) of Trench 4.

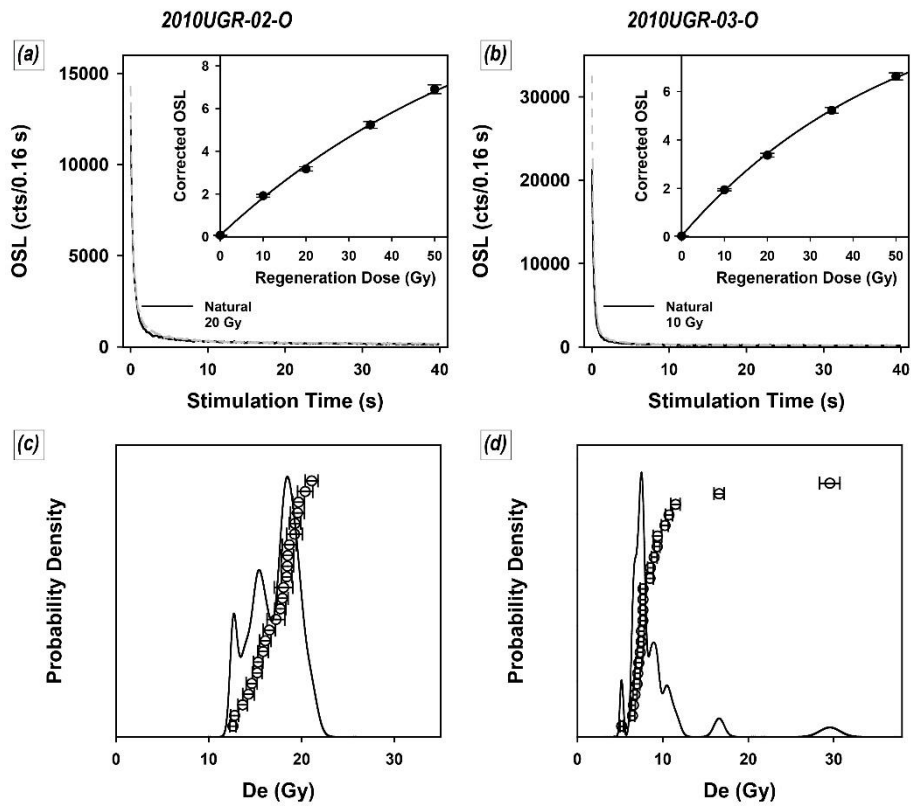


Figure E5: Representative quartz OSL decay curves (a, b) and probability density graph (c, d) of Trench 5.

715

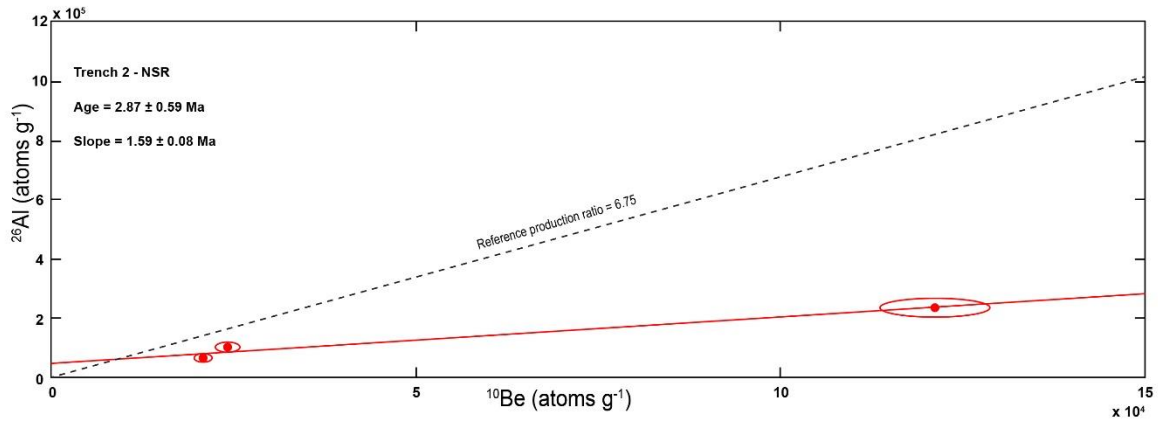


Figure E6:  $^{10}\text{Be}$ - $^{26}\text{Al}$  isochron graph of coring samples in Trench 2.

**Table E1: Dose rates, equivalent doses, and luminescence ages of the samples from the Trench 1**

| Method                             | Sample code  | Dose rate <sup>a</sup><br>(Gy/ka) | Water content <sup>b</sup><br>(%) | Equivalent<br>dose<br>(Gy) | Fading rate<br>(g <sub>2days</sub> , %/dec.) | Aliquots used<br>(n) | age <sup>c</sup><br>(ka, 1σ SE) |
|------------------------------------|--------------|-----------------------------------|-----------------------------------|----------------------------|--|----------------------|---------------------------------|
| Quartz<br>OSL                      | 1803BYG-01-O | 3.26 ± 0.08                       | 13                                | 4.2 ± 0.2                  | -  | 24                   | 1.3 ± 0.1                       |
|                                    | 1803BYG-02-O | 3.54 ± 0.09                       | 16                                | 33 ± 1                     | -  | 24                   | 9 ± 1                           |
|                                    | 1803BYG-03-O | 3.00 ± 0.08                       | 17                                | 31 ± 1                     | -  | 24                   | 10 ± 1                          |
|                                    | 1803BYG-05-O | 3.16 ± 0.08                       | 14                                | 16 ± 1                     | -  | 24                   | 4.9 ± 0.3                       |
|                                    | 1803BYG-06-O | 3.37 ± 0.09                       | 12                                | 11 ± 1                     | -  | 24                   | 3.2 ± 0.2                       |
|                                    | 1803BYG-13-O | 4.02 ± 0.11                       | 13                                | 68 ± 4                     | -  | 24                   | 17 ± 1                          |
|                                    | 1803BYG-14-O | 3.31 ± 0.09                       | 10                                | 27 ± 1                     | -  | 24                   | 8.1 ± 0.3                       |
| K-feldspar<br>pIRIR <sub>225</sub> | 1803BYG-04-O | 3.90 ± 0.09                       | 18                                | 537 ± 23                   | 0.8 ± 0.3                                    | 12                   | 146 ± 8                         |
|                                    | 1803BYG-07-O | 4.36 ± 0.10                       | 16                                | 733 ± 31                   | 0.7 ± 0.2                                    | 12                   | 177 ± 7                         |
|                                    | 1803BYG-08-O | 3.99 ± 0.09                       | 18                                | 558 ± 18                   | 1.1 ± 0.3                                    | 24                   | 151 ± 8                         |
|                                    | 1803BYG-09-O | 4.21 ± 0.10                       | 22                                | 561 ± 21                   | 1.0 ± 0.3                                    | 12                   | 143 ± 7                         |
|                                    | 1803BYG-10-O | 3.95 ± 0.10                       | 20                                | 581 ± 20                   | 1.5 ± 0.3                                    | 12                   | 164 ± 8                         |
|                                    | 1803BYG-11-O | 4.12 ± 0.09                       | 18                                | 594 ± 19                   | 1.0 ± 0.4                                    | 12                   | 155 ± 8                         |
|                                    | 1803BYG-12-O | 4.63 ± 0.11                       | 15                                | 613 ± 21                   | 1.0 ± 0.3                                    | 12                   | 142 ± 7                         |

720 <sup>a</sup> Wet total dose rates. The activities of each radionuclide were converted to dose rates using the data presented by Liritzis et al. (2013). Cosmic ray dose rates were estimated using the method suggested by Prescott and Hutton (1994). The internal dose rate of K-feldspar was calculated assuming internal K content of 12.5 % and by using the methods proposed by Mejdahl (1987) and Readhead (2002). For deriving the total dose rates absorbed by K-feldspar, the internal dose rate of 0.736±0.04 Gy/ka was added to the external ones of each sample.

725 <sup>b</sup> Present water content.

<sup>c</sup> Fading-corrected ages in the case of K-feldspar

**Table E2: Dose rates, equivalent doses, and luminescence ages of the samples from the Trench 2**

| Method        | Sample code  | Dose rate <sup>a</sup><br>(Gy/ka) | Water content <sup>b</sup><br>(%) | Equivalent dose<br>(Gy) | Aliquots used<br>(n) | age <sup>c</sup><br>(ka, 1σ SE) |
|---------------|--------------|-----------------------------------|-----------------------------------|-------------------------|----------------------|---------------------------------|
| Quartz<br>OSL | 1810NSR-05-O | 3.09 ± 0.08                       | 18                                | 9.9 ± 0.8               | 23                   | 3.2 ± 0.3                       |
|               | 1810NSR-06-O | 3.46 ± 0.09                       | 14                                | 12 ± 1                  | 22                   | 3.4 ± 0.4                       |
|               | 1810NSR-07-O | 2.55 ± 0.06                       | 19                                | 47 ± 2                  | 24                   | 19 ± 1                          |

730 <sup>a</sup> Wet total dose rates. The activities of each radionuclide were converted to dose rates using the data presented by Liritzis et al. (2013). Cosmic ray dose rates were estimated using the method suggested by Prescott and Hutton (1994).

<sup>b</sup> Present water content.

**Table E3: Dose rates, equivalent doses, and luminescence ages of the samples from the Trench 3**

| Method                             | Sample code   | Dose rate <sup>a</sup><br>(Gy/ka) | Water content <sup>b</sup><br>(%) | Equivalent<br>dose<br>(Gy) | Fading rate<br>(g <sub>2days</sub> , %/dec.) | Aliquots used<br>(n) | age <sup>c</sup><br>(ka, 1σ SE) |
|------------------------------------|---------------|-----------------------------------|-----------------------------------|----------------------------|--|----------------------|---------------------------------|
| Quartz<br>OSL                      | 1903NS1R-10-O | 3.67 ± 0.09                       | 23                                | 23 ± 1                     | -  | 24                   | 6.4 ± 0.4                       |
| K-feldspar<br>pIRIR <sub>225</sub> | 1903NS1R-02-O | 4.01 ± 0.09                       | 18                                | 606 ± 22                   | 1.8 ± 0.6                                    | 12                   | 173 ± 11                        |
|                                    | 1903NS1R-03-O | 4.11 ± 0.09                       | 16                                | 600 ± 16                   | 2.4 ± 0.4                                    | 12                   | 175 ± 9                         |
|                                    | 1903NS1R-08-O | 4.55 ± 0.10                       | 15                                | 595 ± 18                   | 0.6 ± 0.3                                    | 12                   | 137 ± 6                         |

735 <sup>a</sup> Wet total dose rates. The activities of each radionuclide were converted to dose rates using the data presented by Liritzis et al. (2013). Cosmic ray dose rates were estimated using the method suggested by Prescott and Hutton (1994). The internal dose rate of K-feldspar was calculated assuming internal K content of 12.5 % and by using the methods proposed by Mejdahl (1987) and Readhead (2002). For deriving the total dose rates absorbed by K-feldspar, the internal dose rate of 0.736±0.04 Gy/ka was added to the external ones of each sample.

<sup>b</sup> Present water content.

740 <sup>c</sup> Fading-corrected ages in the case of K-feldspar

**Table E4: Dose rates, equivalent doses, and luminescence ages of the samples from the Trench 4**

| Method        | Sample code  | Dose rate <sup>a</sup><br>(Gy/ka) | Water content <sup>b</sup><br>(%) | Equivalent dose<br>(Gy) | Aliquots used<br>(n) | age <sup>c</sup><br>(ka, 1σ SE) |
|---------------|--------------|-----------------------------------|-----------------------------------|-------------------------|----------------------|---------------------------------|
| Quartz<br>OSL | 2009UGR-05-O | 3.11 ± 0.08                       | 12                                | 3.9 ± 0.1               | 24                   | 1.3 ± 0.1                       |
|               | 2009UGR-06-O | 2.97 ± 0.08                       | 11                                | 3.6 ± 0.1               | 24                   | 1.2 ± 0.1                       |
|               | 2009UGR-07-O | 3.44 ± 0.09                       | 12                                | 0.5 ± 0.1               | 24                   | 0.15 ± 0.03                     |
|               | 2009UGR-08-O | 3.41 ± 0.09                       | 13                                | 0.5 ± 0.1               | 24                   | 0.15 ± 0.03                     |
|               | 2009UGR-09-O | 2.75 ± 0.07                       | 12                                | 16.1 ± 0.9              | 24                   | 5.9 ± 0.4                       |

745 <sup>a</sup> Wet total dose rates. The activities of each radionuclide were converted to dose rates using the data presented by Liritzis et al. (2013). Cosmic ray dose rates were estimated using the method suggested by Prescott and Hutton (1994).

<sup>b</sup> Present water content.

**Table E5: Dose rates, equivalent doses, and luminescence ages of the samples from the Trench 5**

| Method        | Sample code  | Dose rate <sup>a</sup><br>(Gy/ka) | Water content <sup>b</sup><br>(%) | Equivalent dose<br>(Gy) | Aliquots used<br>(n) | age <sup>c</sup><br>(ka, 1σ SE) |
|---------------|--------------|-----------------------------------|-----------------------------------|-------------------------|----------------------|---------------------------------|
| Quartz<br>OSL | 2010UGR-01-O | 3.19 ± 0.08                       | 14                                | 32 ± 3                  | 23                   | 10 ± 1                          |
|               | 2010UGR-02-O | 3.47 ± 0.09                       | 14                                | 17 ± 1                  | 24                   | 4.8 ± 0.2                       |
|               | 2010UGR-03-O | 2.77 ± 0.07                       | 21                                | 7.9 ± 0.3               | 24                   | 2.8 ± 0.1                       |
|               | 2010UGR-04-O | 2.96 ± 0.07                       | 17                                | 7.6 ± 0.2               | 24                   | 2.6 ± 0.1                       |

750 <sup>a</sup> Wet total dose rates. The activities of each radionuclide were converted to dose rates using the data presented by Liritzis et al. (2013). Cosmic ray dose rates were estimated using the method suggested by Prescott and Hutton (1994).

<sup>b</sup> Present water content.

**Data availability.** All detailed age dating data are available in Tables 1-4, E1-E5. Questions or requests for original photomosaic of trenches can be sent to the corresponding author.

755 **Author contributions.** Conceptualization: SH, HCK, Funding acquisition: SM, Investigation: SM, HCK, SL, YBS, JHC, SJK, Project administration: SM, Supervision: SM, Validation: YBS, JGC, SJK, Visualization: SM, SJK, Writing – original draft preparation: SH, Writing – review & editing: SH, YBS, JHC, SM,

**Competing interests.** The authors declare that they have no conflicts of interest.

760

**Financial support.**

This research was supported by a grant (2022-MOIS62-001(RS-2022-ND640011)) of National Disaster Risk Analysis and Management Technology in Earthquake funded by Ministry of Interior and Safety (MOIS, Korea) and supported by the Ministry of Education of the Republic of Korea and the National Research Foundation of Korea (NRF-2023S1A5B5A16080131).

765

## References

- 770 Ansari, K. and Bae, T.S.: Contemporary deformation and strain analysis in South Korea based on long-term (2000–2018) GNSS measurements, *Int. J. Earth Sci. (Geol. Rundsch.)*, 109, 391–405, <https://doi-org-ssl.oca.korea.ac.kr/10.1007/s00531-019-01809-4>, 2020.
- Argus, D.F., Gordon, R.G., Heflin, M.B., Ma, C., Eanes, R.J., Willis, P., Peltier, W.R., and Owen, S.E.: The angular velocities of the plates and the velocity of the Earth's centre from space geodesy, *Geophys. J. Int.*, 18, 1-48, <https://doi:10.1111/j.1365-246X.2009.04463.x>, 2010.
- 775 Ashurkov, S.V., San'kov, V.A., Miroschnichenko, A.I., Likhnev, A.V., Sorokin, A.P., Serov, M.A., and Byzov, L.M.: GPS geodetic constrains on the kinematics of the Amurian Plate, *Russ. Geol. Geophys.*, 52, 239-249, <https://doi.org/10.1016/j.rgg.2010.12.0172>, 2011.
- Atkinson, G.M., Finn, W.D.L. and Charlwood, R.G.: Simple computation of liquefaction probability for seismic hazard applications, *Earthq. Spectra*, 1, 107-123, <https://doi.org/10.1193/1.1585259>, 1984.
- 780 Balco, G., and Rovey, C.W.: An isochron method for cosmogenic-nuclide dating of buried soils and sediments. *Am. J. Sci.*, 308, 1083–1114, <https://doi.org/10.2475/10.2008.02>, 2008.
- Bird, P.: An updated digital model of plate boundaries, *Geochem. Geophys. Geosy.*, 4, 1027, <https://doi.org/10.1029/2001GC000252>, 2003.
- Bonilla, M. G., Mark, R. K., and Lienkaemper, J. J.: Statistical relations among earthquake magnitude, surface rupture length, and surface fault displacement, *B. Seismol. Soc. Am.*, 74, 2379–2411, <https://doi.org/10.1785/BSSA0740062379>, 1984.
- 785 Bronk Ramsey, C.: Methods for summarizing radiocarbon datasets, *Radiocarbon*, 59, 1809-1833, <https://doi.org/10.1017/RDC.2017.108>, 2017.
- Buylaert, J.P., Jain, M., Murray, A.S., Thomsen, K.J., Thiel, C., and Sohbaty, R.: A robust feldspar luminescence dating method for Middle and Late Pleistocene sediments, *Boreas*, 41, 435–451, <https://doi.org/10.1111/j.1502-3885.2012.00248.x>, 2012.
- 790 Buylaert, J.P., Murray, A.S., Thomsen, K.J., and Jain, M.: Testing the potential of an elevated temperature IRSL signal from K-feldspar, *Radiat. Meas.*, 44, 560–565, <https://doi.org/10.1016/j.radmeas.2009.02.007>, 2009.
- Calais, E., Dong, L., Wang, M., Shen, Z., and Vergnolle, M.: Continental deformation in Asia from a combined GPS solution, *Geophys. Res. Lett.*, 33, L24319, <https://doi.org/10.1029/2006GL028433>, 2006.
- Chang, C.-J., and Chang, T.W.: Movement History of the Yangsan Fault based on Paleostress Analysis, *J. Eng. Geo.*, 8, 35-49, 1998.
- 795 Chang, C.-J.: Structural characteristics and evolution of the Yangsan fault, SE Korea, Ph.D. thesis, Kyungpook National University, Korea, 2002.
- Chang, K.H., Woo, B.G., Lee, J.H., Park, S.O., and Yao, A.: Cretaceous and early Cenozoic stratigraphy and history of eastern Kyongsang Basin, S. Korea, *J. Geol. Soc. Korea*, 26, 471-487, 1990.



- Cheon, Y., Cho, H., Ha, S., Kang, H.-C., Kim, J.-S., and Son, M.: Tectonically controlled multiple stages of deformation along the Yangsan Fault Zone, SE Korea, since Late Cretaceous, *J. Asian Earth Sci.*, 170, 188-207, <https://doi.org/10.1016/j.jseaes.2018.11.003>, 2019.
- Cheon, Y., Choi, J.-H., Choi, Y., Bae, H., Han, K.-H., Son, M., Choi, S.-J., and Ryoo, C.-R.: Understanding the distribution and internal structure of the main core of the Yangsan Fault Zone: Current trends and future work, *J. Geol. Soc. Korea*, 56, 61-640, <https://doi.org/10.14770/jgsk.2020.56.5.619>, 2020a.
- 805 Cheon, Y., Choi, J.-H., Kim, N., Lee, H., Choi, I., Bae, H., Rockwell, T.K., Lee, S.R., Ryoo, C.-R., and Choi, H.: Late Quaternary transpressional earthquakes on a long-lived intraplate fault: A case study of the Southern Yangsan Fault, SE Korea, *Quatern. Int.*, 553, 132-143, <https://doi.org/10.1016/j.quaint.2020.07.025>, 2020b.
- Cheon, Y., Ha, S., Lee, S., Cho, H., and Son, M.: Deformation features and history of the Yangsan Fault Zone in the Eonyang-Gyeongju area, SE Korea, *J. Geol. Soc. Korea*, 53, 95-114, <http://doi.org/10.14770/jgsk.2017.53.1.95>, 2017.
- 810 Choi, J.-H., Kim, Y.-S., and Klinger, Y.: Recent progress in studies on the characteristics of surface rupture associated with large earthquakes, *J. Geol. Soc. Korea*, 53, 129-157, <https://doi.org/10.14770/jgsk.2017.53.1.129>, 2017.
- Choi, J.-H., Yang, S.-J., and Kim, Y.-S.: Fault zone classification and structural characteristics of the southern Yangsan fault in the Sangcheon-ri area, SE Korea, *J. Geol. Soc. Korea*, 45, 9-28, 2009.
- Choi, S.-J., Ghim, Y.S., Cheon, Y., and Ko, K.: The First Discovery of Quaternary Fault in the Western Part of the South Yangsan Fault-Sinwoo Site, *Econ. Environ. Geol.*, 52, 251-258, <http://doi.org/10.9719/EEG.2019.52.3.251>, 2019.
- 815 Choi, S.-J., Jeon, J.S., Song, G.Y., Kim, H.C., Kim, Y.H., Choi, B.Y., Chwae, W.C., Han, J.G., Ryoo, C.-R., Sun, C.-G., Jun, M.-S., Kim, G.-Y., Kim, Y. B., Lee, H. J., Shin, J. S., Lee, Y. S., and Kee, W.-S.: Active fault map and seismic hazard map, National Emergency Management Agency, Seoul, Seoul, 939 pp., 2012.
- Crampin, S. and Gao, Y.: Earthquakes can be stress-forecast, *Geophys. J. Int.*, 180, 1124-1127, <https://doi.org/10.1111/j.1365-246X.2009.04475.x>, 2010.
- 820 Delvaux, D., and Sperner, B.: New aspects of tectonic stress inversion with reference to the TENSOR program, in: *New Insights into Structural Interpretation and Modelling*, edited by Nieuwland, D. A., *Geol. Soc., London Spec. Publ.*, 212, 75-100, <https://doi.org/10.1144/GSL.SP.2003.212.01.06>, 2003.
- Delvaux, D., Moeys, R., Stapel, G., Petit, C., Levi, K., Miroshnichenko, A., Ruzhich, V., and San'kov, V.: Paleostress reconstructions and geodynamics of the Baikal region, Central Asia, Part 2. Cenozoic rifting, *Tectonophysics*, 282, 1-38, [https://doi.org/10.1016/S0040-1951\(97\)00210-2](https://doi.org/10.1016/S0040-1951(97)00210-2), 1997.
- 825 DeMets, C., Gordon, R.G., Argus, D.F., and Stein, S.: Current plate motions, *Geophys. J. Int.*, 101, 425-478, <https://doi.org/10.1111/j.1365-246X.1990.tb06579.x>, 1990.
- DeMets, C., Gordon, R.G., Argus, D.F., and Stein, S.: Effect of recent revisions to the geomagnetic reversal time scale on estimates of current plate motions, *Geophys. Res. Lett.*, 21, 191-2,194, <https://doi.org/10.1029/94GL02118>, 1994.
- 830 England, P., and Jackson, J.: Uncharted seismic risk, *Nat. Geosci.*, 4, 348-349, <https://doi.org/10.1038/ngeo1168>, 2011.

- Erlanger, E.D., Granger, D.E., and Gibbon, R.J.: Rock uplift rates in South Africa from isochron burial dating of fluvial and marine terraces, *Geology*, 40, 1019–1022. <https://doi.org/10.1130/G33172.1>, 2012.
- Ge, J., Shi, X., Chen, H., Weldon, R., Walker, R., Li, T., Yang, H., Chen, J., Li, F., Wei, X., Yang, X., Bai, Z., Zhang, Y., Shu, Y., Liu, X., and Yan, Y.: Paleoseismology of the northern Kongur Shan Extensional System, NE Pamir: Implications for potential irregular earthquake recurrence, *J. Geophys. Res.: Solid Earth*, 129, e2023JB028371, <https://doi.org/10.1029/2023JB028371>, 2024.
- Geller, R. J., Jackson, D. D., Kagan, Y. Y., and Mulargia, F.: Earthquakes Cannot Be Predicted, *Science*, 275, 1616-1616, <https://doi.org/10.1126/science.275.5306.1616>, 1997.
- Granger, D. E.: A review of burial dating methods using  $^{26}\text{Al}$  and  $^{10}\text{Be}$ , in: *In Situ-Produced Cosmogenic Nuclides and Quantification of Geological Processes: Geological Society of America Special Paper 415*, edited by: Siame, L. L., Bourlès, D. L., and Brown, 1–16, [https://doi.org/10.1130/2006.2415\(01\)](https://doi.org/10.1130/2006.2415(01)), 2006.
- Granger, D.E., and Muzikar, P.F.: Dating sediment burial with in situ-produced cosmogenic nuclides: Theory, techniques, and limitations, *Earth Planet. Sc. Lett.*, 188, 269-281, [https://doi.org/10.1016/S0012-821X\(01\)00309-0](https://doi.org/10.1016/S0012-821X(01)00309-0), 2001.
- Gurpinar, A.: The importance of paleoseismology in seismic hazard studies for critical facilities, *Tectonophysics*, 408, 23-28, <https://doi.org/10.1016/j.tecto.2005.05.042>, 2005.
- Gwon, O., Park, K., Naik, S. P., Shin, H.-C., and Kim, Y. -S.: A study on the characteristics of fault activity in the southern part of the Ulsan fault using paleoseismic method, *J. Geol. Soc. Korea*, 57, 109-121, <https://doi.org/10.14770/jgsk.2021.57.2.109>, 2021.
- Gwon, S., Cho, S., Park, D., Choi, W.-H., Nakao, R., Tanaka, T., and Inoue, D.: Microscopic analysis of fault rock using X-ray computed tomography from the Wolsan trench in the middle part of Yangsan fault, SE Korea, *J. Geol. Soc. Korea*, 56, 273-284, <https://doi.org/10.14770/jgsk.2020.56.2.273>, 2020.
- Ha, S., Son, M., and Seong, Y.B.: Active Fault Trace Identification Using a LiDAR High-Resolution DEM: A Case Study of the Central Yangsan Fault, Korea, *Remote Sens.*, 14, 4838, <https://doi.org/10.3390/rs14194838>, 2022.
- Han, J.-W., Lee, S., Ha, S., Lee, C. H., Seong, Y. B., Kang, H.-C., Kim, M.-C., Gil, T., and Son, M.: A preliminary study on the Quaternary faulting along the northern part of Yangsan Fault and Yeongdeok Fault, in: *76th Annual Meeting of the Geological Society of Korea and 2021 Fall Joint Conference of the Geological Sciences*, Jeju, Korea, 26-28 October 2021, 317, 2021.
- Han, M., Kim, K.-H., Son, M., Kang, S.Y., and Park, J.-H.: Location of recent micro earthquakes in the Gyeongju area, *Geophysics Geophys. Explor.*, 19, 97-104, <https://doi.org/10.7582/GGE.2016.19.2.097>, 2016.
- Hansen, V., Murray, A., Buylaert, J.-P., Yeo, E.Y., and Thomsen, K.: A new irradiated quartz for beta source calibration, *Radiat. Meas.*, 81, 123–127, <https://doi.org/10.1016/j.radmeas.2015.02.017>, 2015.
- Heki, K., Miyazaki, S., Takahashi, H., Kasahara, M., Kimata, F., Miura, S., Vasilenko, N.F., Ivashchenko, A., and An, K.-D.: The Amurian Plate motion and current plate kinematics in eastern Asia, *J. Geophys. Res.*, 104, 29, 147-29, 155, <https://doi.org/10.1029/1999JB900295>, 1999.

- 865 Hong, T. K., Lee, J., and Hough, S. E.: Long-term evolution of intraplate seismicity in stress shadows after a megathrust, *Phys. Earth Planet. In.*, 245, 59–70, <https://doi.org/10.1016/j.pepi.2015.05.009>, 2015.
- Hong, T. K., Lee, J., Park, S., and Kim, W.: Time-advanced occurrence of moderate-size earthquakes in a stable intraplate region after a megathrust earthquake and their seismic properties, *Sci. Rep.*, 8, 13331, <https://doi.org/10.1038/s41598-018-31600-5>, 2018.
- 870 Hong, Y., OH J.-S., Hong S.-C., and Shin J.: Geomorphological Development and Fault Activity of the Central-Southern Yangsan Fault (I): Developmental Characteristics and Distribution of the Quaternary Landforms, *J. Korean Geomorphological Assoc.*, 28, 67-81. <https://doi.org/10.16968/JKGA.28.1.67>, 2021.
- Hough, S., and Page, M.: Toward a consistent model for strain accrual and release for the New Madrid seismic zone, central United States, *J. Geophys. Res.*, 116, B03311. <http://dx.doi.org/10.1029/2010JB007783>, 2011.
- 875 Hough, S.E., Armbruster, J.G., Seeber, L., and Hough, J.F.: On the modified Mercalli intensities and magnitudes of the 1811–1812 New Madrid earthquakes, *J. Geophys. Res.*, 105(B10), 23,839–23,864, <https://doi.org/10.1029/2000JB900110>, 2000.
- Hwang, B.-H., Lee, J. D., and Yang, K.: Petrological study of the granitic rocks around the Yangsan Fault: Lateral displacement of the Yangsan Fault, *J. Geol. Soc. Korea*, 40, 161–178, 2004.
- Hwang, B. H., Lee, J. D., Yang, K., and McWilliams, M.: Cenozoic strike-slip displacement along the Yangsan Fault, southeast  
880 Korean Peninsula, *Int. Geol. Rev.*, 49, 768–775, <https://doi.org/10.2747/0020-6814.49.8.768>, 2007a.
- Hwang, B. H., McWilliams, M., Son, M., and Yang, K.: Tectonic implication of A-type granites across the Yangsan Fault, Gigyae and Gyeongju areas, southeast Korean Peninsula, *Int. Geol. Rev.*, 49, 1094–1102, <https://doi.org/10.2747/0020-6814.49.12.1094>, 2007b.
- Ikeya, M., Miki, T., and Tanaka, K.: Dating of a Fault by Electron Spin Resonance on Intrafault Materials, *Science*, 215, 1392-  
885 1393, <https://doi.org/10.1126/science.215.4538.1392>, 1982.
- Jin, K., Kim, Y.-S., Kang, H.C. and Shin, H.C.: Study on developing characteristics of the Quaternary Gusan Fault in Uljin, Gyeongbuk, Korea, *J. Geol. Soc. Korea*, 49, 197-207, <https://doi.org/10.14770/jgsk.2013.49.2.197>, 2013.
- Johnston, A.C., and Schweig, E.S.: The enigma of the New Madrid earthquakes of 1811–1812, *Annu. Rev. Earth Pl. Sc.*, 24, 339-384, <https://doi.org/10.1146/annurev.earth.24.1.339>, 1996.
- 890 Kanamori, H.: The energy release in great earthquakes, *J. Geophys. Res.*, 82, 2981–2987, <https://doi.org/10.1029/JB082i020p02981>, 1977.
- Kang, H.-C., Cheon, Y., Ha, S., Seo, K., Kim, J.-S., Shin, H. C., and Son, M.: Geology and U-Pb Age in the Eastern Part of Yeongdeok-gun, Gyeongsangbuk-do, Korea, *J. Petrological Soc. Korea*, 27, 153-171, <https://doi.org/10.7854/JPSK.2018.27.3.15>, 2018.
- 895 Kee, W.-S., Kim, Y.-H., Lee, H.-J., Choi, D.-L., Kim, B.-C., Song, K.-Y., Koh, H.-J., Lee, S.R., Yeon, Y.G., Hwang, S.-H., Sung, N.-H.: South eastern fault variable research and DB Construction, Korea Institute of Geoscience and Mineral Resources, Daejeon, 327 pp., 2009.

- Khromovskikh, V. S.: Determination of magnitudes of ancient earthquakes from dimensions of observed seismodislocations, *Tectonophysics*, 166, 269-280, [https://doi.org/10.1016/0040-1951\(89\)90219-9](https://doi.org/10.1016/0040-1951(89)90219-9), 1989.
- 900 Kim, C.-M., Cheon, Y., Lee, T.-H., Choi, J.-H., Ha, S., and Jeong, J. O.: Long-Term Weakening Processes and Short-Term Seismic Slip Behavior of an Intraplate Mature Fault Zone: A Case Study of the Yangsan Fault, SE Korea, *J. Geophys. Res-Sol Ea*, 127, e2021JB023154, <https://doi.org/10.1029/2021JB023154>, 2022.
- Kim, C.-M., Ha, S., and Son, M.: Evidence of coseismic slip recorded by Quaternary fault materials and microstructures, Naengsuri, Pohang, *J. Geol. Soc. Korea*, 56, 175-192, <https://doi.org/10.14770/jgsk.2020.56.2.175>, 2020a.
- 905 Kim, C.-M., Jeong, J. O., Gu, D., and Han, H.: Identification of materials in principal slip zones of faults by X-ray diffraction analysis using a small amount of sample, *J. Geol. Soc. Korea*, 53, 873-883, <http://doi.org/10.14770/jgsk.2017.53.6.873>, 2017a.
- Kim, D.-E., and Seong, Y.B.: Cumulative Slip Rate of the Southern Yangsan Fault from Geomorphic Indicator and Numerical Dating, *J. Kor. Geogr. Soc.*, 56, 201-213. <https://doi.org/10.22776/KGS.2021.56.2.201>, 2021.
- Kim, D. E., and Oh, J.-S.: Landform Classification Using Geomorphons on the Middle Yangsan Fault System, Southeastern  
910 Korea, *J. Korean Geogr. Soc.*, 54, 493-505, 2019.
- Kim, D.H., Hwang, J.H., Park, K.H., and Song, K.Y.: Explanatory Note of The Pusan Sheet, 1:1:250,000, Korea Institute of Energy and Resources, Daejeon, 1998.
- Kim, H.-U., and Bae, T.-S.: Monitoring of Possible Activities of Yangsan Fault Zone Using GNSS, *Appl. Sci.*, 13, 1862, <https://doi.org/10.3390/app13031862>, 2023.
- 915 Kim, I.-S.: Origin and tectonic evolution of the East Sea (Sea of Japan) and the Yangsan fault system: a new synthetic interpretation, *J. Geol. Soc. Korea*, 28, 84-109, 1992.
- Kim, K.-H., Ree, J.-H., Kim, Y., Kim, S., Kang, S.Y., and Seo, W.: Assessing whether the 2017  $M_w$  5.4 Pohang earthquake in South Korea was an induced event, *Science*, 360, 1007-1009, <https://doi.org/10.1126/science.aat6081>, 2018.
- Kim, K.-H., Seo, W., Hang, J., Kwon, J., Kang, S.Y., Ree, J.-H., Kim, S., and Liu, K.: The 2017  $M_L$  5.4 Pohang earthquake  
920 sequence, Korea, recorded by a dense seismic network, *Tectonophysics*, 774, 228306, <https://doi.org/10.1016/j.tecto.2019.228306>, 2020b.
- Kim, M.-C., Jung, S., Yoon, S., Jeong, R.-Y., Song, C.W., and Son, M.: Neotectonic crustal deformation and current stress field in the Korean Peninsula and Their Tectonic Implications: a review, *J. Petrological Soc. Korea*, 25, 169-193, <https://doi.org/10.7854/JPSK.2016.25.3.169>, 2016.
- 925 Kim, M.-J., and Lee, H.-K.: Long-term patterns of earthquakes influenced by climate change: Insights from earthquake recurrence and stress field changes across the Korean Peninsula during interglacial periods, *Quaternary Sci. Rev.*, 321, 108369, <https://doi.org/10.1016/j.quascirev.2023.108369>, 2023
- Kim, M.-J., and Lee, H.-W.: ESR dating of fault gouge - review, *J. Geol. Soc. Korea*, 56, 175-192, <https://doi.org/10.14770/jgsk.2020.56.2.211>, 2020.

- 930 Kim, N., Choi, J.-H., Park, S.-I., Lee, T.-H. and Choi, Y.: Cumulative offset analysis of the Central-Southern Yangsan Fault based on topography of Quaternary fluvial terrace, *J. Geol. Soc. Korea*, 56, 135-154, <https://doi.org/10.14770/jgsk.2020.56.2.135>, 2020c.
- Kim, N., Park, S.-I., and Choi, J.-H.: Internal architecture and earthquake rupture behavior of a long-lived intraplate strike-slip fault: A case study from the Southern Yangsan Fault, Korea, *Tectonophysics*, 816, 229006, 935 <https://doi.org/10.1016/j.tecto.2021.229006>, 2021.
- Kim, T., Choi, J.-H., Cheon, Y., Lee, T.-H., Kim, N., Lee, H., Kim, C.-M., Choi, Y., Bae, H., Kim, S.-G., Ryoo, C.-R., and Klinger, Y.: Correlation of paleoearthquake records at multiple sites along the southern Yangsan Fault, Korea: Insights into rupture scenarios of intraplate strike-slip earthquakes, *Tectonophysics*, 854, 229817, <https://doi.org/10.1016/j.tecto.2023.229817>, 2023.
- 940 Kim, T., Lee, H., Kim, D. E., Choi, J. H., Choi, Y., Han, M., and Kim, Y. S.: Determination of the long-term slip rate of a fault in a slowly deforming region based on a reconstruction of the landform and provenance, *Geomorphology*, 461, 109286, <https://doi.org/10.1016/j.geomorph.2024.109286>, 2024.
- Kim, Y.-S., Jin, K., Choi, W.-H., and Kee, W.-S.: Understanding of active faults: A review for recent researches, *J. Geol. Soc. Korea*. 47, 723-752, 2011.
- 945 Kim, Y.-S., Kim, T., Kyung, J. B., Cho, C. S., Choi, J.-H., Choi, C. U.: Preliminary study on rupture mechanism of the 9.12 Gyeongju Earthquake, *J. Geol. Soc. Korea*, 53, 407-422, <https://doi.org/10.14770/jgsk.2017.53.3.407>, 2017b.
- Ko, K., Choi, S.-J., Lee, T.-H., Gihm, Y. S., Kim, C.-M., Kim, K., and Cheon, Y.: A multidisciplinary approach to characterization of the mature northern Yangsan fault in Korea and its active faulting, *Mar. Geophys. Res.*, 43, 21, <https://doi.org/10.1007/s11001-022-09486-w>, 2022.
- 950 Korea Meteorological Administration: 2022 yearbook, Korea Meteorological Administration, Seoul, 416 pp., 2022. Retrieved from <https://www.kma.go.kr> (archived on 6/March/2023).
- Kreutzer, S.: calc\_FadingCorr(): Apply a fading correction according to Huntley and Lamothe (2001) for a given g-value and a given tc. Function version 0.4.3, in *Luminescence*, edited by Kreutzer, S., Burow, C., Dietze, M., Fuchs, M.C., Schmidt, C., Fischer, M., Friedrich, J., Mercier, N., Philippe, A., Riedesel, S., Autzen, M., Mittelstrass, D., Gray, H.J., and Galharret, J., 955 <https://CRAN.R-project.org/package=Luminescence> (last access: January 2024), 2023.
- Kuwahara, Y., Choi, J.-H., Cheon, Y., and Imanishi, K.: Dependence of earthquake faulting type on fault strike across the Korean Peninsula: Evidence for weak faults and comparison with the Japanese Archipelago, *Tectonophysics*, 804, 228757, <https://doi.org/10.1016/j.tecto.2021.228757>, 2021.
- 960 Kyung, J.B.: Paleoseismology of the Yangsan Fault, southeastern part of the Korean Peninsula, *Ann. Geophys.*, 46, 983-996, <http://hdl.handle.net/2122/999>, 2003.

- Lal, D.: Cosmic ray labeling of erosion surfaces: in situ nuclide production rates and erosion models, *Earth Planet. Sc. Lett.*, 104, 424–439, [https://doi.org/10.1016/0012-821X\(91\)90220-C](https://doi.org/10.1016/0012-821X(91)90220-C), 1991.
- Lee, C. H., Seong Y. B., Oh, J.-S., Kim, D. E.: Tectonic Geomorphology on Yugye-Bogyongsan Area of Yangsan Fault Zone, *J. Korean Geomorphological Assoc.*, 26, 93-106, <https://doi.org/10.16968/JKGA.26.1.93>, 2019.
- 965 Lee, H.-K., and Schwarcz, H. P.: ESR dating of the subsidiary faults in the Yangsan Fault System, Korea, *Quaternary Sci. Rev.*, 20, 999–1003, [https://doi.org/10.1016/S0277-3791\(00\)00055-X](https://doi.org/10.1016/S0277-3791(00)00055-X), 2001.
- Lee, H.K., and Yang, J.S.: ESR dating of the Eupchon fault, south Korea, *Quat. Geochronol.*, 2, 392–397, <https://doi.org/10.1016/j.quageo.2006.04.009>, 2003.
- 970 Lee, J., Rezaei, S., Hong, Y., Choi, J.-H., Choi, J.-H., Choi, W.-H., Rhee, K.-W., and Kim, Y.-S.: Quaternary fault analysis through a trench investigation on the northern extension of the Yangsan fault at Dangu-ri, Gyungju-si, Gyeongsangbuk-do, *J. Geol. Soc. Korea*, 51, 471-485, <https://doi.org/10.14770/jgsk.2015.51.5.471>, 2015.
- Lee, K.: Historical earthquake data of Korean. *J. Korea Geophys. Soc.* 1, 3-22, 1998.
- Lee, K., and Yang, W.-S.: Historical Seismicity of Korea, *B. Seismol. Soc. Am.*, 96, 846-855, <https://doi.org/10.1785/0120050050>, 2006.
- 975 Lee, S.: Characteristics of the Quaternary Faults in SE Korea: Insight from the Yangsan Fault and Gokgang Fault, Ph.D. thesis, Pusan National University, Korea, 184 pp., 2023.
- Lee, S., Han, J., Ha, S., Lim, H., Seong, Y. B., Choi, J.-H., Lee, C. H., Kim, S.-J., Kang, H.-C., Kim, M.-C., Lim, H., and Son, M.: Characteristics of the Quaternary faulting detected along the Yangsan Fault in Yugye- and Jungsan-ri, northern Pohang City, *J. Geol. Soc. Korea*, 58, 427-443, <http://doi.org/10.14770/jgsk.2022.58.4.427>, 2022.
- 980 Lee, Y., Cheon, Y., Ha, S., Kang, H.-C., Choi, J.-H., and Son, M.: Geometric and kinematic characteristics of the Quaternary fault at Seoee site, in Goseong-gun, Gyeongsangnam-do, *J. Geol. Soc. Korea*, 53, 115-127, <https://doi.org/10.14770/jgsk.2017.53.1.115>, 2017.
- Lim, H., Ha, S., Ryoo, C.-R., Lee, T.-H., and Son, M.: Evidence of surface rupture in the southernmost part of the Yangsan fault and deterministic seismic hazard assessment: in the Busan metropolitan area, in: 76th Annual Meeting of the Geological Society of Korea and 2021 Fall Joint Conference of the Geological Sciences, Jeju, Korea, 26-28 October 2021, 275, 2021.
- 985 Liu, J., Ren, Z., Min, W., Ha, G., and Lei, J.: The advance in obtaining fault slip rate of strike slip fault-A review. *Earthq. Res. Adv.*, 1, 100032. <https://doi.org/10.1016/j.egrea.2021.100032>, 2021.
- Liu, M., and Stein, S.: Mid-continental earthquakes: Spatiotemporal occurrences, causes, and hazards, *Earth-Sci. Rev.*, 162, 364–386, <https://doi.org/10.1016/j.earscirev.2016.09.016>, 2016.
- 990 Mason, D.B.: Earthquake magnitude potential of the Intermountain Seismic Belt, USA, from surface-parameter scaling of late Quaternary faults. *B. Seismol. Soc. Am.*, 86, 1487–1506, <https://doi.org/10.1785/BSSA0860051487>, 1996.

- McCalpin, J.P.: Application of Paleoseismic Data to Seismic Hazard Assessment and Neotectonic Research, in: Paleoseismology, 2nd ed., edited by McCalpin, J.P., Academic Press-Elsevier, Burlington, USA, 1–106, 1995. [https://doi.org/10.1016/S0074-6142\(09\)95009-4](https://doi.org/10.1016/S0074-6142(09)95009-4), 2009.
- Min, Z., Hu, G., Jiang, X., Liu, S., and Yang, Y.: Catalog of Chinese Historic Strong Earthquakes From 23 AD to 1911, Seismological Press, Beijing, China, 514 pp., 1995.
- Murray, A. S., and Wintle, A. G.: Luminescence dating of quartz using an improved single-aliquot regenerative-dose protocol, *Radiat. Meas.*, 32, 57-73, [https://doi.org/10.1016/S1350-4487\(99\)00253-X](https://doi.org/10.1016/S1350-4487(99)00253-X), 2000.
- 1000 Murray, J., and Langbein, J.: Slip on the San Andreas Fault at Parkfield, California, over Two Earthquake Cycles, and the Implications for Seismic Hazard, *B.Seismol. Soc. Am.*, 96, S283–S303, <https://doi.org/10.1785/0120050820>, 2006.
- Naik, S. P., Rockwell, T. K., Jeong, S. H., Kim, Y. S., Shin, H. C., Choi, J. H., Ha, S., and Son, M.: Evidence for large Holocene earthquakes along the Yangsan fault in the SE Korean Peninsula revealed in three-dimensional paleoseismic trenches, *Geol. Soc. Am. Bull.*, online publication, <https://doi.org/10.1130/B37275.1>, 2024.
- 1005 O'Neill, C., Müller, D., and Steinberger, B.: On the uncertainties in hot spot reconstructions and the significance of moving hot spot reference frames, *Geochem. Geophys. Geosy.*, 6, <https://doi.org/10.1029/2004GC000784>, 2005.
- Obara, K., and Kato, A.: Connecting slow earthquakes to huge earthquakes. *Science*, 353, 6296, <https://doi.org/10.1126/science.aaf1512>, 2016.
- Park, C., and Lee, G.: Analysis on Fault-Related Landforms in the Gyeongju Area of the Yangsan Fault Valley, *J. Korean Geomorphological Assoc.*, 25, 19-30, <https://doi.org/10.16968/JKGA.25.1.19>, 2018.
- 1010 Park, J. C., Kim, W., Chung, T. W., Baag, C. E., and Ree, J. H.: Focal mechanism of recent earthquakes in the Southern Korean Peninsula, *Geophys. J. Int.*, 169, 1103–1114, <https://doi.org/10.1111/j.1365-246X.2007.03321.x>, 2007.
- Park, Y., Ree, J.-H., and Yoo, S.-H.: Fault slip analysis of Quaternary faults in southeastern Korea, *Gondwana Res.*, 9, 118–125, <https://doi.org/10.1016/j.gr.2005.06.007>, 2006.
- 1015 Patyniak, M., Landgraf, A., Dzhumabaeva, A., Abdrakhmatov, K. E., Rosenwinkel, S., Korup, O., Preusser, F., Fohmeister, J., Arrowsmith, J.R., and Strecker, M. R.: Paleoseismic record of three Holocene earthquakes rupturing the Issyk-Ata fault near Bishkek, North Kyrgyzstan, *Bull. Seismol. Soc. Am.*, 107, 2721-2737, <https://doi.org/10.1785/0120170083>, 2017.
- Powell, R. E., and Weldon II, R. J.: Evolution of the San Andreas fault, *Annu. Rev. Earth Pl. Sc.*, 20, 431-468, <https://doi.org/10.1146/annurev.ea.20.050192.002243>, 1992.
- 1020 Reimer, P., Austin, W., Bard, E., Bayliss, A., Blackwell, P., Bronk Ramsey, C., and Talamo, S.: The IntCal20 Northern Hemisphere Radiocarbon Age Calibration Curve (0–55 cal kBP), *Radiocarbon*, 62, 725–757, <https://doi.org/10.1017/RDC.2020.41>, 2020.
- Reiter, L.: *Earthquake Hazard Analysis: Issue and Insights*. Columbia University Press, New York, USA, 254 pp., 1990.

- Ryoo, C.-R., and Cheon, Y.: Characteristics of the Main Fault Zone Developed Along Yangsan Fault: On the Outcrop of  
1025 Cheonjeon-ri, Dudong-myeon, Ulju-gun, Ulsan, Korea, *J. Petrological Soc. Korea*, 28, 347-357,  
<https://doi.org/10.7854/JPSK.2019.28.4.347>, 2019.
- Ryoo, C.-R., Lee, B.-J., Cho, D.-L., Chwae, U.-C., Choi, S.-J., and Kim J.-Y.: Quaternary fault of Dangu-ri in Gyeongju  
Gangdong-myeon: Byeokgye Fault, in: Spring Joint Conference on East-North Asia Ore deposit of Cause of Formation, The  
Korean Society of Economic and Environmental Geology/The Korean Society of Mineral and Energy Resources  
1030 Engineers/Korean Society of Earth and Exploration Geophysicists, 1999.
- Sadler, P.: The Influence of Hiatuses on Sediment Accumulation Rates, *GeoResearch Forum*, 5, 15-40, 1999.
- Schellart, W. P., and Rawlinson, N.: Convergent plate margin dynamics: New perspectives from structural geology, geophysics  
and geodynamic modelling, *Tectonophysics*, 483, 4-19, <https://doi.org/10.1016/j.tecto.2009.08.030>, 2010.
- Seno, T., Sakurai, T., and Stein, S.: Can the Okhotsk plate be discriminated from the North American plate?, *J. Geophys. Res.-*  
1035 *Sol. Ea.*, 101(B5), 11305-11315, <https://doi.org/10.1029/96JB00532>, 1996.
- Seno, T., Stein, S., and Gripp, A. E.: A model for the motion of the Philippine Sea plate consistent with NUVEL-1 and  
geological data, *J. Geophys. Res.- Sol. Ea.*, 98(B10), 17941-17948, <https://doi.org/10.1029/93JB00782>, 1993.
- Shimazaki, K., and Nakata, T.: Time-predictable recurrence model for large earthquakes, *Geophys. Res. Lett.*, 7, 279-282,  
<https://doi.org/10.1029/GL007i004p00279>, 1980.
- 1040 Sim, H., Song, Y., Son, M., Park, C., and Choi, W.: Reactivated Timings of Yangsan Fault in the Northern Pohang Area,  
Korea, *Econ. Environ. Geol.*, 50, 97-104, <https://doi.org/10.9719/EEG.2017.50.2.97>, 2017.
- Smith, B. R., and Sandwell, D. T.: A model of the earthquake cycle along the San Andreas Fault System for the past 1000  
years, *J. Geophys. Res.*, 111, B01405. <https://doi.org/10.1029/2005JB003703>, 2006.
- Soh, I., Chang, C., Lee, J., Hong, T.-K., and Park, E.-S.: Tectonic stress orientations and magnitudes, and friction of faults,  
1045 deduced from earthquake focal mechanism inversions over the Korean Peninsula, *Geophys. J. Int.*, 123, 1360–  
1373, <https://doi.org/10.1093/gji/ggy061>, 2018. Sohn, D.-H., Choi, B.-K., Kim, S., Park, S.-C., Lee, W.-J., and Park, P.-H.:  
Decaying Post-Seismic Deformation Observed on the Korean Peninsula Following the 2011 Tohoku-Oki  
Earthquake, *Sensors*, 21, 4493, <https://doi.org/10.3390/s21134493>, 2021.
- Son, M., Song, C.W., Kim, M.-C., Cheon, Y., Cho, H., and Sohn, Y.K.: Miocene tectonic evolution of the basins and fault  
1050 systems, SE Korea: dextral, simple shear during the East Sea (Sea of Japan) opening, *J. Geol. Soc. London*, 172, 664-680,  
<https://doi.org/10.1144/jgs2014-079>, 2015.
- Song, C.W.: Study on the evolution of the Miocene Pohang Basin based on its structural characteristics, Ph.D. thesis, Pusan  
National University, Korea, 146 pp., 2015.
- Song, Y., Ha, S., Lee, S., Kang, H.-C., Choi, J.-H., and Son, M.: Quaternary structural characteristics and paleoseismic  
1055 interpretation of the Yangsan Fault at Dangu-ri, Gyeongju-si, SE Korea, through trench survey, *J. Geol. Soc. Korea*, 56, 155–  
173, <https://doi.org/10.14770/jgsk.2020.56.2.155>, 2020.



- Song, Y., Park, C., Sim, H., Choi, W., and Son, M.: Reactivated Timings of Yangsan Fault in the Sangcheon-ri Area, Korea, *Econ. Environ. Geol.*, 49, 97-104, <https://doi.org/10.9719/EEG.2016.49.2.97>, 2016.
- 1060 Song, Y., Sim, H., Hong, S., and Son, M.: K-Ar Age-dating Results of Some Major Faults in the Gyeongsang Basin: Spatio-temporal Variability of Fault Activations during the Cenozoic Era, *Econ. Environ. Geol.*, 52, 449-457, <https://doi.org/10.9719/EEG.2019.52.5.449>, 2019.
- Suzuki, Y., Nakata, T., Watanabe, M., Battulga, S., Enkhtaivan, D., Demberel, S., Odonbaatar, C., Bayasgalan, A., and Badral, T.: Discovery of Ulaanbaatar Fault: A new earthquake threat to the capital of Mongolia, *Seismol. Soc. Am.*, 92, 437-447, <https://doi.org/10.1785/0220200109>, 2021. Talwani, P.: On the nature of intraplate earthquakes, *J. Seismol.*, 21, 47-68, 1065 <https://doi.org/10.1007/s10950-016-9582-8>, 2017.
- Uchida, N., and Burgmann, R.: Repeating Earthquakes, *Annu. Rev. Earth Pl. Sc.*, 47, 305-332, <https://doi.org/10.1146/annurev-earth-053018-060119>, 2019.
- Wells, D. L., and Coppersmith, K. J.: New empirical relationships among magnitude, rupture length, rupture width, rupture area, and surface displacement, *B. Seismol. Soc. Am.*, 84, 974-1002, <https://doi.org/10.1785/BSSA0840040974>, 1994.
- 1070 Woith, H., Petersen G.M., Hainzl, S., and Dahm, T.: Review: Can Animals Predict Earthquakes?, *B. Seismol. Soc. Am.*, 108, 1031-1045, <https://doi.org/10.1785/0120170313>, 2018.
- Wolin, E., Stein, S., Pazzaglia, F., Meltzer, A., Kafka, A., and Berti, C.: Mineral, Virginia, earthquake illustrates seismicity of a passive-aggressive margin, *Geophys. Res. Lett.*, 39, L02305, <https://doi.org/10.1029/2011GL050310>, 2012. Woo, J.-U., Rhie, J., Kim, S., Kang, T.-S., Kim, K.-H., and Kim, Y.H.: The 2016 Gyeongju earthquake sequence revisited: aftershock 1075 interactions within a complex fault system, *Geophys. J. Int.*, 217, 58-74, <https://doi.org/10.1093/gji/ggz009>, 2019.
- Woo, S., Lee, H., Han, R., Chon, C.-M., Son, M., and Song, I.: Frictional properties of gouges collected from the Yangsan Fault, SE Korea. *J. Geol. Soc. Korea*, 51, 569-584, <https://doi.org/10.14770/jgsk.2015.51.6.569>, 2015.
- Wyss, M.: Cannot Earthquakes Be Predicted?, *Science*, 278, 487-490, <https://doi.org/10.1126/science.278.5337.48>, 1997.
- Xu, S., Nieto-Samaniego, A.F., and Alaniz-Àlvarez, S.A.: Quantification of true displacement using apparent displacement 1080 along an arbitrary line on a fault plane, *Tectonophysics*, 467, 107-118, <https://doi.org/10.1016/j.tecto.2008.12.004>, 2009.
- Yang, J.-S., and Lee, H.-K.: ESR dating of fault gouge from the Gacheon 1 site on the Yangsan fault zone, *J. Geol. Soc. Korea*, 48, 459-472, 2012.